Journal of Minerals and Materials Characterization and Engineering, 2026, 14(6), 145-179
https://www.scirp.org/journal/jmmce
ISSN Online: 2327-4085
ISSN Print: 2327-4077

Comparative Micromechanical Analysis of Interfacial Transition Zone Effects on Stiffness and Thermal Conductivity in Cementitious Composites

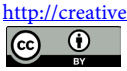
Koffi Apélété Konde[1,2*], Komi Apélété Amou[1,2], Kossi Tepe[1,2]

[1]Department of Physics, University of Lomé, Lomé, Togo
[2]Laboratoire de l'Énergie Solaire (LES), Lomé, Togo
Email: *gatienk89@gmail.com

How to cite this paper: Konde, K.A., Amou, K.A. and Tepe, K. (2026) Comparative Micromechanical Analysis of Interfacial Transition Zone Effects on Stiffness and Thermal Conductivity in Cementitious Composites. *Journal of Minerals and Materials Characterization and Engineering*, **14**, 145-179.
https://doi.org/10.4236/jmmce.2026.146011

Received: August 26, 2026
Accepted: November 21, 2026
Published: November 24, 2026

Copyright © 2026 by author(s) and Scientific Research Publishing Inc.
This work is licensed under the Creative Commons Attribution International License (CC BY 4.0).
http://creativecommons.org/licenses/by/4.0/



Open Access

Abstract

The prediction of the effective thermomechanical properties of heterogeneous composites is essential for the design and optimization of cement-based materials with improved durability and energy performance. In this study, a micromechanical framework based on Eshelby's equivalent inclusion theory and the Mori-Tanaka homogenization scheme is proposed to jointly estimate the effective Young's modulus and the effective thermal conductivity of particulate composites. The model considers spherical inclusions embedded in a continuous matrix and is extended to account for the presence of an interfacial transition zone (ITZ) surrounding the inclusions, via the Hervé-Zaoui coated-inclusion model. Three microstructural architectures are compared: an ideal single-inclusion system, a fully ITZ-affected core-shell system, and a mixed system combining both populations. The predicted effective properties are verified against the Hashin-Shtrikman and Voigt-Reuss bounds. The comparison is carried out at matched Young's-modulus and conductivity ratios: the inclusion-to-matrix and ITZ-to-matrix ratios of E and of λ are set equal, whereas the bulk- and shear-modulus ratios remain conditional on the adopted Poisson's ratios. The aggregate-core volume fraction f_a is held fixed across the architectures and the ITZ fraction is reported separately, so that the differences isolate the effect of the ITZ from that of a reduced aggregate content. At $f_a = 0.6$ (ITZ fraction 0.22), the ITZ reduces the effective Young's modulus by 9.4% and the effective thermal conductivity by 7.6%. The gap of 1.8 percentage points is modest and sensitive to the residual mismatch of the inputs: it falls to about 0.9 points when the ITZ contrasts and the Poisson's ratios are matched exactly. It is consistent with the two-channel (spherical and deviatoric) nature of mechanical load transfer as opposed to the single-channel na-

ture of thermal conduction. The conductivity reduction is a loss for conductive applications but a benefit for insulating concretes, whereas the stiffness reduction is a loss in both cases. The mixed inclusion system roughly halves both reductions (to 4.8% and 3.9%), offering a lever to balance structural stiffness against thermal insulation in cementitious composites. At high inclusion content the results are Mori-Tanaka estimates for a continuous matrix and are not validated against dense coated or mixed packings.

Keywords

Micromechanics, Interfacial Transition Zone, Cementitious Composites, Mori-Tanaka Scheme, Effective Young's Modulus, Effective Thermal Conductivity

1. Introduction

The thermal comfort of buildings is a major challenge that civil engineering researchers have been facing for some time, while also considering the mechanical strength of the material. According to a recent study, an empirical relationship between these two quantities (thermal conductivity and compressive strength) has been confirmed for insulating concrete, and the most effective foaming methods and lightweight aggregates for reconciling insulation and strength have been identified [1]. Experimental work on expanded polystyrene-based composites confirms this compromise: the use of an ultra-high-performance concrete matrix limits the drop in mechanical strength induced by the addition of insulating inclusions [2].

Cementitious composite materials, such as mortar and concrete, must therefore meet two often conflicting requirements: high compressive strength and good thermal insulation performance. These two macroscopic properties depend directly on the heterogeneous microstructure of the material [3] [4], and in particular on the interface between the aggregates and the cement paste that coats them. This interface hosts an interfacial transition zone (ITZ), a thin, highly porous layer whose stiffness and thermal conductivity are both markedly lower than those of the sound cement paste, so that it degrades the load-transfer capacity and the heat-conduction capacity of the composite simultaneously [5] [6]. The ITZ remains recognized today as the most vulnerable component of cementitious composites, and recent work using synchrotron X-ray microtomography has made it possible to directly characterize its volumetric structure and its influence on the mechanical behavior of mortar [7]. A recent review likewise confirms that the ITZ remains the weakest region of concrete, owing to its thinness and high porosity, which promotes crack propagation through the least resistant areas [8]. Its presence is known to lead to a significant overestimation of the effective properties when neglected in micromechanical models [9].

Classical homogenization schemes—Eshelby's inclusion theory [10], self-con-

sistent schemes, and the Mori-Tanaka scheme [11] [12]—have extensively addressed the mechanical effect of the ITZ. From a thermal perspective, an extension of the Mori-Tanaka scheme accounting for interfacial contact resistance and particle size distributions has also been proposed [13], but it models the interface as a contact conductance rather than as a separate third phase with its own properties. Recent work has combined multiphase inclusion theory with finite element simulations to evaluate the influence of the ITZ on the mechanical properties of recycled concrete, explicitly distinguishing several ITZs according to the nature (old or new) of the mortar and aggregates [14]. On the thermal side, recent mesostructural approaches have developed effective thermal conductivity models that account for the ITZ volume fraction and aggregate morphology, based on random packings of superellipsoidal particles [15].

While the literature offers advanced mechanical and thermal models, these are almost always treated in isolation, with distinct microstructural assumptions and, critically, distinct property contrasts. Comparing the two degradations therefore requires more than computing them within a single framework: it requires probing both fields at the same contrast levels, since the magnitude of an ITZ-induced loss depends strongly on how far the inclusion and the interphase differ from the matrix. The contribution of the present work is precisely this controlled comparison. A single coated-inclusion architecture is used to compute both effective properties, the inclusion-to-matrix and ITZ-to-matrix ratios of Young's modulus and of thermal conductivity are matched between the two fields, the aggregate-core fraction is held fixed across architectures, and a differential sensitivity indicator is introduced to measure whether the ITZ still reduces one property more than the other once these sources of bias have been controlled. Based on Eshelby's theory [10], the Mori-Tanaka scheme [11], and the Hervé-Zaoui embedded inclusion model [16], the effective Young's modulus and the effective thermal conductivity of a cementitious composite are evaluated jointly under three architectures (simple, core-shell, and mixed).

2. Theoretical Background

The micromechanics of composite materials establishes mathematical models linking microscopic properties and behaviors to effective macroscopic properties [17], based on the assumption of scale separation. This approach defines a Representative Volume Element (RVE) large enough to statistically represent the microstructure and small enough to be considered a material point at the macroscopic scale [18]. The goal is to homogenize this RVE in order to calculate the effective properties of the composite.

Figure 1 illustrates this principle. A heterogeneous body of macroscopic size L (left) is described, at each material point, by an RVE of characteristic size l (right) containing inclusions of size d. The RVE is then replaced by an equivalent homogeneous material whose effective properties are obtained by homogenization, which is valid provided that the scale separation condition $d \ll l \ll L$ is satisfied.

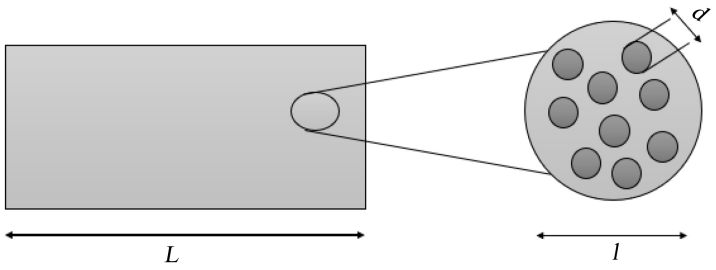


Figure 1. Diagram of a representative volume element (RVE) and the equivalent homogeneous material. Scale separation condition $d \ll l \ll L$.

2.1. Eshelby Problem

Eshelby's inclusion problem (1957) is a cornerstone of composite micromechanics [19]. It provides an analytical solution for the strain and stress fields of an ellipsoidal inclusion subjected to an eigenstrain $\boldsymbol{\varepsilon}^*$, serving as the basis for homogenization schemes such as the Mori-Tanaka and self-consistent schemes [20] [21]. The two formulations of Eshelby fundamentally used in micromechanics, namely the inclusion problem and the inhomogeneity problem, are succinctly described below and used for the remainder of this work.

For the inclusion problem, Eshelby introduces into a closed medium Ω considered infinite, elastic, homogeneous, and isotropic, characterized by its stiffness tensor $\mathbb{C}_0$ an ellipsoidal region possessing the same elastic properties as the matrix but subjected to a uniform eigenstrain $\boldsymbol{\varepsilon}^*$. The internal stress field is then obtained using Hooke's law:

$$\boldsymbol{\sigma}^{\text{in}} = \mathbb{C}_0 : \left(\boldsymbol{\varepsilon}^{\text{in}} - \boldsymbol{\varepsilon}^*\right), \tag{1}$$

with $\mathbb{C}_0$ the stiffness tensor of the infinite medium, $\boldsymbol{\varepsilon}^{\text{in}}$ the internal strain tensor of the inclusion, an $\boldsymbol{\varepsilon}^*$ the eigenstrain tensor. The field induced by an eigenstrain, as demonstrated by Eshelby for an ellipsoidal inclusion, remains constant within it. It is related to the Eshelby tensor (a fourth-order tensor) by

$$\boldsymbol{\varepsilon}^{\text{in}} = \mathbb{S} : \boldsymbol{\varepsilon}^* \tag{2}$$

with $\mathbb{S}$ the isotropic Eshelby tensor, expressed as a linear combination of volumetric and deviatoric projectors for an elastic matrix [22]:

$$\mathbb{S} = s_1 \mathbb{J} + s_2 \mathbb{K} \tag{3}$$

where the projector tensors are defined by

$$\mathbb{J} = \frac{1}{3} \boldsymbol{I} \otimes \boldsymbol{I}, \quad \mathbb{K} = \mathbb{I}_s - \mathbb{J}, \tag{4}$$

with $\mathbb{I}_s$ the symmetric identity of order four. The coefficients s_1 and s_2 depend solely on the elastic properties of the matrix:

$$s_1 = \frac{3k_0}{3k_0 + 4\mu_0}, \quad s_2 = \frac{6\left(k_0 + 2\mu_0\right)}{5\left(3k_0 + 4\mu_0\right)}. \tag{5}$$

Thus, the explicit expression for the Eshelby tensor of a spherical inclusion in an isotropic matrix is

$$\mathbb{S}^{\text{sph}} = \frac{3k_0}{3k_0 + 4\mu_0}\mathbb{J} + \frac{6\left(k_0 + 2\mu_0\right)}{5\left(3k_0 + 4\mu_0\right)}\mathbb{K}. \tag{6}$$

For an elastic inclusion different from the matrix (the inhomogeneity problem), a uniform average strain $\overline{\boldsymbol{\varepsilon}}$ is applied at infinity in order to determine the average strain and stress within the inclusion. Applying Eshelby's equivalence principle [10], the average strain within the inclusion is written as

$$\boldsymbol{\varepsilon}^{\text{int}} = \overline{\boldsymbol{\varepsilon}} + \mathbb{S} : \boldsymbol{\varepsilon}^{*}, \tag{7}$$

where $\mathbb{S}$ is the Eshelby tensor associated with the matrix. The average stress in the inclusion then satisfies

$$\boldsymbol{\sigma}^{\text{int}} = \mathbb{C}_i : \left(\boldsymbol{\varepsilon}^{\text{int}} - \boldsymbol{\varepsilon}^{*}\right). \tag{8}$$

By imposing continuity of stresses between the real problem and the equivalent problem, a relation is obtained that eliminates the eigenstrain $\boldsymbol{\varepsilon}^{*}$. After some algebraic manipulation, the average strain in the inclusion is written

$$\boldsymbol{\varepsilon}^{\text{int}} = \left[\mathbb{I} + \mathbb{S} : \mathbb{C}_0^{-1} : \left(\mathbb{C}_i - \mathbb{C}_0\right)\right]^{-1} : \overline{\boldsymbol{\varepsilon}}. \tag{9}$$

Introducing the Hill tensor

$$\mathbb{P} = \mathbb{S} : \mathbb{C}_0^{-1}, \tag{10}$$

the previous equation becomes

$$\boldsymbol{\varepsilon}^{\text{int}} = \left[\mathbb{I} + \mathbb{P} : \left(\mathbb{C}_i - \mathbb{C}_0\right)\right]^{-1} : \overline{\boldsymbol{\varepsilon}}. \tag{11}$$

The tensor in brackets is the *dilute strain localization tensor*, denoted

$$\mathbb{A}_i^{\text{dil}} = \left[\mathbb{I} + \mathbb{P} : \left(\mathbb{C}_i - \mathbb{C}_0\right)\right]^{-1}, \tag{12}$$

so that the average strain in the inclusion takes the compact form

$$\boldsymbol{\varepsilon}^{\text{int}} = \mathbb{A}_i^{\text{dil}} : \overline{\boldsymbol{\varepsilon}}. \tag{13}$$

2.2. Mori-Tanaka Scheme

Several homogenization models (rule of mixtures, Hashin-Shtrikman bounds, Maxwell, self-consistent, Mori-Tanaka) allow the effective mechanical and thermal properties of a heterogeneous material to be estimated from the properties of its constituents and their microstructure. In the present study, the Mori-Tanaka scheme was chosen because it accommodates coated inclusions naturally, and therefore an explicit interfacial transition zone, while remaining fully analytical.

Each inclusion is subjected to the average strain of the matrix rather than to the global macroscopic strain [11]. Consider a material composed of a matrix of stiffness $\mathbb{C}_0$ and one or more families of inclusions of stiffness $\mathbb{C}_i$, present with volume fractions f_i. The Eshelby tensor $\mathbb{S}_i$ associated with the shape of the inclusion is evaluated from the properties of the matrix. The average strain in an inclusion of type i is written

$$\boldsymbol{\varepsilon}_i = \mathbb{T}_i : \boldsymbol{\varepsilon}_0, \tag{14}$$

where $\boldsymbol{\varepsilon}_0$ denotes the average strain in the matrix and $\mathbb{T}_i$ is the dilute localiza-

tion tensor of the inclusion,

$$\mathbb{T}_i = \left[\mathbb{I} + \mathbb{S}_i : \mathbb{C}_0^{-1} : \left(\mathbb{C}_i - \mathbb{C}_0\right)\right]^{-1}. \tag{15}$$

The macroscopic strain $\boldsymbol{E}$ follows from the volume average condition:

$$\boldsymbol{E} = f_0\boldsymbol{\varepsilon}_0 + \sum_i f_i\boldsymbol{\varepsilon}_i. \tag{16}$$

Substituting the expression for $\boldsymbol{\varepsilon}_i$ and solving for $\boldsymbol{\varepsilon}_0$ gives

$$\boldsymbol{\varepsilon}_0 = \left(f_0\mathbb{I} + \sum_i f_i\mathbb{T}_i\right)^{-1} : \boldsymbol{E}. \tag{17}$$

The strain localization tensor in the Mori-Tanaka scheme is then

$$\mathbb{A}_i^{\mathrm{MT}} = \mathbb{T}_i : \left(f_0\mathbb{I} + \sum_j f_j\mathbb{T}_j\right)^{-1}, \tag{18}$$

and the effective stiffness tensor of the composite is obtained from the weighted average of the local stiffnesses:

$$\tilde{\mathbb{C}} = \mathbb{C}_0 + \sum_i f_i\left(\mathbb{C}_i - \mathbb{C}_0\right) : \mathbb{A}_i^{\mathrm{MT}}. \tag{19}$$

3. Application to the Three Inclusion Architectures

3.1. Description of the Composite Microstructure

At the mesoscopic scale considered here, mortar is described as a cement paste matrix containing siliceous aggregates. Three microstructural configurations are analysed: simple inclusions, multilayer (coated) composite inclusions, and a mixture of the two populations. For the sake of modelling simplicity, all aggregates are treated as spherical inclusions surrounded by a shell of uniform thickness representing the ITZ. Figure 2 presents the simplified RVE model of the composite material under study.

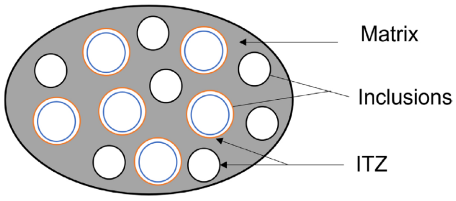


Figure 2. Simplified representation of an RVE of the composite material.

3.2. Elastic Formulation

To determine the homogenized macroscopic properties, the problem is posed in the following form:

$$\begin{cases} \operatorname{div}\boldsymbol{\sigma}(\boldsymbol{x}) = 0 & (V) \quad (\mathrm{a}) \\ \boldsymbol{\sigma}(\boldsymbol{x}) = \mathbb{C}(\boldsymbol{x}) : \boldsymbol{\varepsilon}(\boldsymbol{x}) & (V) \quad (\mathrm{b}) \\ \boldsymbol{\varepsilon} = \dfrac{1}{2}\left(\nabla\boldsymbol{u} + \nabla\boldsymbol{u}^{\mathrm{T}}\right) & (V) \quad (\mathrm{c}) \\ \boldsymbol{u}(\boldsymbol{x}) = \boldsymbol{E}\cdot\boldsymbol{x} & (\partial V) \quad (\mathrm{d}) \end{cases} \tag{20}$$

where Equation (20a) represents the microscopic-scale equilibrium equation with $\boldsymbol{\sigma}(\boldsymbol{x})$ the local stress field, while Equation (20b) defines the linear elastic behavior of the phases ($\mathbb{C}$ being the fourth-order stiffness tensor). The strain field $\boldsymbol{\varepsilon}$ is related to the displacement field $\boldsymbol{u}(\boldsymbol{x})$ through the kinematic relation given in Equation (20c). Finally, Equation (20d) prescribes the homogeneous macroscopic strain $\boldsymbol{E}$ on the boundary of the RVE, which yields the classical average relation $\langle\boldsymbol{\varepsilon}\rangle_V = \boldsymbol{E}$. This step connects local mechanical fields to macroscopic average quantities. For an RVE of volume V and boundary ∂V, the equations of linear elasticity govern the local behavior [23].

3.3. Thermal Formulation

The micromechanical model is extended to thermal conduction using Fourier's law:

$$\begin{cases} \operatorname{div}\boldsymbol{q}(\boldsymbol{x}) = 0 & (V) \quad (\mathrm{a}) \\ \boldsymbol{q}(\boldsymbol{x}) = -\boldsymbol{\lambda}(\boldsymbol{x})\cdot\boldsymbol{g}(\boldsymbol{x}) & (V) \quad (\mathrm{b}) \\ \boldsymbol{g}(\boldsymbol{x}) = \nabla T(\boldsymbol{x}) & (V) \quad (\mathrm{c}) \\ T(\boldsymbol{x}) = \boldsymbol{G}\cdot\boldsymbol{x} & (\partial V) \quad (\mathrm{d}) \end{cases} \tag{21}$$

where Equation (21a) represents steady-state heat flux conservation in the absence of internal heat sources, $\boldsymbol{q}(\boldsymbol{x})$ being the local heat flux vector. Equation (21b) expresses Fourier's law, with $\boldsymbol{\lambda}(\boldsymbol{x})$ the second-order local thermal conductivity tensor of the phases. The local temperature gradient vector $\boldsymbol{g}(\boldsymbol{x})$ is defined in Equation (21c). Finally, Equation (21d) prescribes a linear temperature boundary condition on ∂V, where $\boldsymbol{G}$ is the constant macroscopic temperature gradient. Under these conditions the average relation $\langle\boldsymbol{g}\rangle_V = \boldsymbol{G}$ is strictly satisfied.

3.4. Treatment of Single, Double, and Mixed Inclusions

The theoretical tools introduced above (the Eshelby inclusion problem, localization tensors, the Mori-Tanaka scheme, and the Hervé-Zaoui analytical model) are now applied to the three cases studied. The approach begins with the representation of the RVEs of the three microstructural configurations, followed by the homogenization of the multilayer inclusions using the Hervé-Zaoui model [16], and finally by the homogenization of the RVE with the Mori-Tanaka scheme [11].

3.4.1. Single Family of Inclusions

We consider an RVE composed of an isotropic elastic matrix (tensor $\mathbb{C}_0$) and a family of isotropic spherical inclusions (tensor $\mathbb{C}_i$, volume fraction f_i) as illustrated in **Figure 3**. The interface is perfectly bonded. The macroscopic homogenized behavior is defined by

$$\boldsymbol{\Sigma} = \tilde{\mathbb{C}} : \boldsymbol{E} \tag{22}$$

In the isotropic case, the fourth-order stiffness tensor is written as

$$\mathbb{C} = 3k\mathbb{J} + 2\mu\mathbb{K} \tag{23}$$

with $\mathbb{J}$ and $\mathbb{K}$ given in Equation (4). Under the Mori-Tanaka scheme, the effective stiffness tensor is expressed as

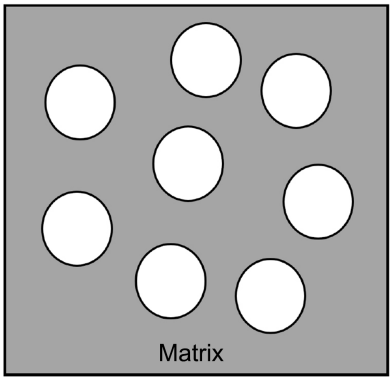


Figure 3. Simplified representation of an RVE with a single family of inclusions.

$$\tilde{\mathbb{C}} = \mathbb{C}_0 + \sum_i f_i \left(\mathbb{C}_i - \mathbb{C}_0\right) : \mathbb{A}_i^{\mathrm{MT}} = 3k^{\mathrm{eff}}\mathbb{J} + 2\mu^{\mathrm{eff}}\mathbb{K} \tag{24}$$

where $\mathbb{A}_i^{\mathrm{MT}}$ is given by Equation (18) and

$$k^{\mathrm{eff}} = k_0 + \frac{f_i\left(k_i - k_0\right)}{1 + \left(1 - f_i\right)\dfrac{k_i - k_0}{k_0 + \dfrac{4}{3}\mu_0}} \tag{25}$$

$$\mu^{\mathrm{eff}} = \mu_0 + \frac{f_i\left(\mu_i - \mu_0\right)}{1 + \left(1 - f_i\right)\dfrac{\mu_i - \mu_0}{\mu_0 + \beta_0}} \tag{26}$$

$$\beta_0 = \mu_0 \frac{6\left(k_0 + 2\mu_0\right)}{5\left(3k_0 + 4\mu_0\right)} \tag{27}$$

$$E^{\mathrm{eff}} = \frac{9k^{\mathrm{eff}}\mu^{\mathrm{eff}}}{3k^{\mathrm{eff}} + \mu^{\mathrm{eff}}} \tag{28}$$

3.4.2. Coated (Core-Shell) Inclusions

We now consider an RVE composed of a matrix and coated spherical inclusions, as illustrated in Figure 4. The Hervé-Zaoui model gives the stiffness tensor of the composite inclusion, which is then treated as a simple inclusion in the Mori–Tanaka scheme. The effective stiffness tensor of the composite is written as

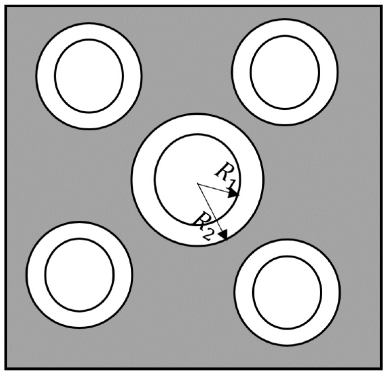


Figure 4. RVE with spherical composite (coated) inclusions.

$$\tilde{\mathbb{C}} = \mathbb{C}_0 + \sum_i f_i \left(\mathbb{C}_{\text{inc}} - \mathbb{C}_0\right) : \mathbb{A}_i^{\text{MT}} \tag{29}$$

where $\mathbb{C}_0$ is the stiffness tensor of the matrix and f_i the volume fraction of the inclusions. When the phases are isotropic, the scalar expressions (25)-(26) are recovered, the properties of the original inclusion being replaced by those of the homogeneous equivalent phase $\mathbb{C}_{\text{inc}}$.

In order to determine this stiffness tensor, the biphasic composite inclusion is immersed in an infinite matrix, as illustrated in Figure 5. The outer radii of these phases satisfy $0 = R_0 < R_1 < R_2 < \infty$.

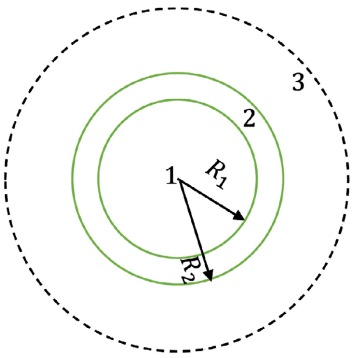


Figure 5. The three-phase model.

Hydrostatic loading. Under hydrostatic loading, spherical symmetry dictates a purely radial displacement field in each phase i:

$$u_r^{(i)}(r) = F_i r + \frac{G_i}{r^2} \tag{30}$$

where F_i and G_i are real constants to be determined. The volumetric strain and the components of the stress tensor are then

$$\theta^{(i)} = 3F_i, \quad \sigma_{rr}^{(i)} = 3k_i F_i - \frac{4\mu_i G_i}{r^3}, \quad \sigma_{\theta\theta}^{(i)} = \sigma_{\phi\phi}^{(i)} = 3k_i F_i + \frac{2\mu_i G_i}{r^3} \tag{31}$$

The boundary conditions require $G_1 = 0$ (regularity at the center) and $F_3 = \sigma_0/(9k_3)$ (macroscopic hydrostatic loading $\sigma_0 \boldsymbol{I}$ at infinity). At each interface $r = R_k$ ($k = 1, 2$), continuity of the radial displacement and of the radial stress is written in matrix form:

$$\begin{pmatrix} R_k & \frac{1}{R_k^2} \\ 3k_k & -\frac{4\mu_k}{R_k^3} \end{pmatrix} \begin{pmatrix} F_k \\ G_k \end{pmatrix} = \begin{pmatrix} R_k & \frac{1}{R_k^2} \\ 3k_{k+1} & -\frac{4\mu_{k+1}}{R_k^3} \end{pmatrix} \begin{pmatrix} F_{k+1} \\ G_{k+1} \end{pmatrix} \tag{32}$$

Inverting system (32) gives the transfer matrix between adjacent phases:

$$\begin{pmatrix} F_{k+1} \\ G_{k+1} \end{pmatrix} = \frac{1}{3k_{k+1} + 4\mu_{k+1}} \begin{pmatrix} 3k_k + 4\mu_{k+1} & \frac{4(\mu_{k+1} - \mu_k)}{R_k^3} \\ 3(k_{k+1} - k_k) R_k^3 & 3k_{k+1} + 4\mu_k \end{pmatrix} \begin{pmatrix} F_k \\ G_k \end{pmatrix} \tag{33}$$

For the two-layer case, propagation through the two interfaces leads to

$$\begin{pmatrix} F_3 \\ G_3 \end{pmatrix} = \boldsymbol{N}^{(2)}\boldsymbol{N}^{(1)}\begin{pmatrix} F_1 \\ 0 \end{pmatrix} = \boldsymbol{Q}^{(2)}\begin{pmatrix} F_1 \\ 0 \end{pmatrix} = \begin{pmatrix} Q_{11}^{(2)}F_1 \\ Q_{21}^{(2)}F_1 \end{pmatrix} \tag{34}$$

with, after evaluation of the matrix product $\boldsymbol{Q}^{(2)} = \boldsymbol{N}^{(2)}\boldsymbol{N}^{(1)}$,

$$Q_{11}^{(2)} = \frac{3k_1 + 4\mu_2}{3k_2 + 4\mu_2}, \quad Q_{21}^{(2)} = \frac{3R_1^3\left(k_2 - k_1\right)}{3k_2 + 4\mu_2} \tag{35}$$

The macroscopic homogeneity condition requires the perturbation term in the matrix to vanish, hence $G_3 = 0$. Applying the transfer relation at the interface R_2 and using the coefficients in Equation (35), we obtain

$$3\left(k_3 - k_2\right)R_2^3 Q_{11}^{(2)} + \left(3k_3 + 4\mu_2\right)Q_{21}^{(2)} = 0 \tag{36}$$

Identifying $k_3 = k_{\text{eff}}$ and solving Equation (36), the effective bulk modulus of the coated inclusion is

$$k_{\text{eff}} = \frac{3k_2R_2^3Q_{11}^{(2)} - 4\mu_2Q_{21}^{(2)}}{3\left(R_2^3Q_{11}^{(2)} + Q_{21}^{(2)}\right)} \tag{37}$$

Introducing the volume fractions $f_1 = R_1^3/R_2^3$ and $f_2 = 1 - f_1$, this expression can be recast in the compact recursive form

$$k_{\text{eff}} = k_2 + \frac{f_1}{\dfrac{1}{k_1 - k_2} + \dfrac{3f_2}{3k_2 + 4\mu_2}} \tag{38}$$

Deviatoric loading. For a purely deviatoric loading, characterized by $\operatorname{tr}(\boldsymbol{\varepsilon}) = 0$, the displacement field depends on both the radial and angular coordinates. In spherical coordinates (r, θ, ϕ), for an axisymmetric loading, the general solution in each phase i is

$$\begin{cases} 2u_r^{(i)}(r,\theta) = \left(A_i r + \dfrac{B_i}{r^4} + C_i r^3 + \dfrac{D_i}{r^2}\right)P_2(\cos\theta) \\ u_\theta^{(i)}(r,\theta) = \left(E_i r + \dfrac{F_i}{r^4} + G_i r^3 + \dfrac{H_i}{r^2}\right)\dfrac{\mathrm{d}P_2(\cos\theta)}{\mathrm{d}\theta} \end{cases} \tag{39}$$

where $P_2(\cos\theta) = \frac{1}{2}\left(3\cos^2\theta - 1\right)$ is the Legendre polynomial of order 2. The regularity conditions at the center require $B_1 = D_1 = F_1 = H_1 = 0$. At infinity, the asymptotic behavior must be compatible with the applied macroscopic loading. The equilibrium equations in the absence of body forces establish linear relations between the integration constants, thereby reducing the number of independent parameters to four per phase.

The continuity conditions at the interfaces $r = R_k$ lead to a matrix system analogous to the hydrostatic case:

$$\boldsymbol{M}_k(R_k)\boldsymbol{W}_k = \boldsymbol{M}_{k+1}(R_k)\boldsymbol{W}_{k+1} \tag{40}$$

where $\boldsymbol{W}_k = \left(A_k, B_k, C_k, D_k\right)^{\mathrm{T}}$ groups the independent constants of phase k and $\boldsymbol{M}_k$ denotes the associated local matrix. Solving this system yields the transfer matrix $\boldsymbol{T}^{(k)}$ relating two adjacent phases:

$$\boldsymbol{W}_{k+1} = \boldsymbol{T}^{(k)}\boldsymbol{W}_k \tag{41}$$

For the two-layer case, propagation through both layers reads

$$\boldsymbol{W}_3 = \boldsymbol{T}^{(2)}\boldsymbol{T}^{(1)}\boldsymbol{W}_1 = \boldsymbol{S}^{(2)}\boldsymbol{W}_1 \tag{42}$$

The homogeneity condition in the matrix, equivalent to cancelling the decaying perturbation terms, leads to a second-degree algebraic equation in μ_{eff}/μ_2 [16]:

$$A\left(\frac{\mu_{\text{eff}}}{\mu_2}\right)^2 + B\left(\frac{\mu_{\text{eff}}}{\mu_2}\right) + C = 0 \tag{43}$$

whose physically admissible root is

$$\mu_{\text{eff}} = \mu_2 \frac{-B + \sqrt{B^2 - 4AC}}{2A} \tag{44}$$

The coefficients A, B, and C depend on the elastic properties (k_i, μ_i, ν_i) and the radii (R_1, R_2) of the two layers, and are given by [16]

$$A = R_2^5(1-2\nu_2)(7-10\nu_2)Z_{12} + 10R_2^2\left(7-12\nu_2+8\nu_2^2\right)Z_{22} \tag{45}$$

$$B = 3R_2^5(1-2\nu_2)(15\nu_2-7)Z_{12} - 20R_2^2(1-2\nu_2)^2 Z_{22} \tag{46}$$

$$C = -R_2^5(1-2\nu_2)(7+5\nu_2)Z_{12} + 10R_2^2\left(7-\nu_2^2\right)Z_{22} \tag{47}$$

where Z_{12} and Z_{22} are second-order minors of the accumulated transfer matrix $\boldsymbol{S}^{(2)}$ of Equation (42); their explicit definition is given in Appendix B, together with the equivalent closed-form solution of Christensen and Lo [12] for the particular case of a single coating.

3.5. Mixed Inclusions

Consider an RVE containing both simple and coated spherical inclusions, as illustrated in **Figure 6**.

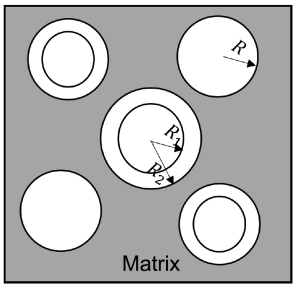


Figure 6. RVE with mixed inclusions.

The overall effective stiffness tensor of the composite is

$$\tilde{\mathbb{C}} = \mathbb{C}_0 + \sum_i f_i\left(\tilde{\mathbb{C}}_i - \mathbb{C}_0\right) : \mathbb{A}_i^{\text{MT}} \tag{48}$$

where $\tilde{\mathbb{C}}_i$ is either the stiffness tensor of a bare inclusion or that of an equivalent coated inclusion, $\mathbb{C}_0$ is the stiffness tensor of the matrix phase, and f_i is the volume fraction of each distinct population.

3.6. Extension to the Thermal Conductivity Problem

The thermal transport properties of the homogeneous, isotropic phases are characterized by a conductivity tensor $\boldsymbol{\lambda}_i$ ($i=1,2,3$), which reduces to $\boldsymbol{\lambda}_i=\lambda_i\boldsymbol{I}$. The local boundary value problem governing steady-state conduction in the domain Ω is

$$\begin{cases} \operatorname{div}\boldsymbol{q}(\boldsymbol{x})=0 & (\Omega) \quad (\mathrm{a}) \\ \boldsymbol{q}(\boldsymbol{x})=-\boldsymbol{\lambda}(\boldsymbol{x})\cdot\nabla T(\boldsymbol{x}) & (\Omega) \quad (\mathrm{b}) \\ T(\boldsymbol{x})=\boldsymbol{G}^{\infty}\cdot\boldsymbol{x} & (\partial\Omega) \quad (\mathrm{c}) \end{cases} \tag{49}$$

where $T(\boldsymbol{x})$ is the temperature field, $\boldsymbol{q}(\boldsymbol{x})$ the heat flux vector, and $\boldsymbol{G}^{\infty}=G^{\infty}\boldsymbol{e}_1$ the prescribed uniform macroscopic temperature gradient on $\partial\Omega$. Assuming a homogeneous isotropic phase, substituting (49b) into (49a) yields the Laplace equation

$$\Delta T(\boldsymbol{x})=0 \tag{50}$$

Following Caré and Hervé [24], the solution T_i and the radial heat flux q_r^i take the general form

$$\begin{cases} T_i(r,\theta)=\left(\alpha_i r+\dfrac{\beta_i}{r^2}\right)\cos\theta \\ q_r^i(r,\theta)=-\lambda_i\left(\alpha_i-\dfrac{2\beta_i}{r^3}\right)\cos\theta \end{cases} \tag{51}$$

where α_i and β_i are integration constants determined from the boundary and interface continuity conditions.

3.6.1. Determination of the Constants α_i and β_i

For a two-layer coated inclusion (core: phase 1; shell/ITZ: phase 2; matrix: phase 3), six constants $(\alpha_1,\alpha_2,\alpha_3,\beta_1,\beta_2,\beta_3)$ must be determined.

Boundary conditions at the origin and at infinity. In the core region ($0\le r\le R_1$),

$$T_1=\left(\alpha_1 r+\frac{\beta_1}{r^2}\right)\cos\theta,\quad q_r^1=-\lambda_1\left(\alpha_1-\frac{2\beta_1}{r^3}\right)\cos\theta\quad(0\le r\le R_1) \tag{52}$$

To avoid a singularity at the origin,

$$\beta_1=0 \tag{53}$$

and imposing the far-field condition $T_3\sim G^{\infty}r\cos\theta$ as $r\to\infty$ gives

$$\alpha_3=G^{\infty}\quad(\text{i.e. }\alpha_3'=1) \tag{54}$$

Continuity at the interface $r=R_1$**.** Continuity of T and q_r requires

$$\alpha_1=\alpha_2+\frac{\beta_2}{R_1^3} \tag{55}$$

and

$$\lambda_1\alpha_1=\lambda_2\left(\alpha_2-\frac{2\beta_2}{R_1^3}\right) \tag{56}$$

Continuity at the interface $r=R_2$**.** Similarly,

$$\alpha_2 + \frac{\beta_2}{R_2^3} = G^\infty + \frac{\beta_3}{R_2^3} \tag{57}$$

and

$$\lambda_2\left(\alpha_2 - \frac{2\beta_2}{R_2^3}\right) = \lambda_3\left(G^\infty - \frac{2\beta_3}{R_2^3}\right) \tag{58}$$

Equations (55), (56), (57) and (58) form a linear system of four equations in the four unknowns $(\alpha_1, \alpha_2, \beta_2, \beta_3)$. Defining the conductivity ratios $X = \lambda_2/\lambda_1$ and $Y = \lambda_3/\lambda_2$, the exact analytical expressions for these constants read

$$\alpha_1 = \underbrace{\left(\frac{-6XYR_2^3}{(1-X)(2Y-2)R_1^3 - (1+2Y)(1+2X)R_2^3}\right)}_{=\alpha_1'} G^\infty \tag{59}$$

$$\alpha_2 = \underbrace{\left(\frac{-3YR_2^3(1+2X)}{(1-X)(2Y-2)R_1^3 - (1+2Y)(1+2X)R_2^3}\right)}_{=\alpha_2'} G^\infty \tag{60}$$

$$\beta_2 = \underbrace{\left(\frac{3YR_1^3R_2^3(1-X)}{(1-X)(2Y-2)R_1^3 - (1+2Y)(1+2X)R_2^3}\right)}_{=\beta_2'} G^\infty \tag{61}$$

and finally

$$\beta_3 = \underbrace{\left(\frac{-3YR_2^6 + 3Y(1-X)R_1^3R_2^3}{(1-X)(2Y-2)R_1^3 - (1+2Y)(1+2X)R_2^3} - R_2^3\right)}_{=\beta_3'} G^\infty \tag{62}$$

3.6.2. Averages over the Coated Inclusion

Following Herve [25] and Caré and Hervé [24], the volume averages over the coated inclusion (domain Ω_{inc}) of the temperature gradient and of the heat flux take the form

$$\langle \nabla T \rangle_{\Omega_{\text{inc}}} = \left(\alpha_3' + \frac{\beta_3'}{R_2^3}\right) G^\infty \boldsymbol{e}_1; \quad \langle \boldsymbol{q} \rangle_{\Omega_{\text{inc}}} = -\lambda_3\left(\alpha_3' + \frac{\beta_3'}{R_2^3}\right) G^\infty \boldsymbol{e}_1 \tag{63}$$

where λ_3 denotes the conductivity of the surrounding phase, which in the equivalent-inclusion approach of Section 3.6.3 is precisely the quantity to be identified.

3.6.3. Equivalent Conductivity of the Coated Inclusion

The constants determined in Section 3.6.1 fully describe the temperature field inside the two-layer inclusion. In order to feed this information into the Mori–Tanaka scheme, the coated inclusion (core λ_1 of radius R_1, ITZ shell λ_2 of outer radius R_2) must first be replaced by an equivalent homogeneous sphere of conductivity λ_{eq}.

The equivalence condition is that the temperature field outside R_2 be left unperturbed when the coated inclusion is replaced by the equivalent sphere, *i.e.* $\beta_3 = 0$ for $\lambda_3 = \lambda_{\text{eq}}$. Introducing the dimensionless quantities

$$f_1 = \left(\frac{R_1}{R_2}\right)^3, \quad u = \frac{\beta_2}{\alpha_2 R_2^3}, \tag{64}$$

where f_1 is the volume fraction of the core within the coated inclusion, the continuity conditions (55)-(56) reduce to the single scalar relation

$$u = f_1 \frac{\lambda_2 - \lambda_1}{\lambda_1 + 2\lambda_2}. \tag{65}$$

Writing the equality of the flux-to-temperature ratio at $r = R_2$ between the coated inclusion and the equivalent sphere gives $\lambda_{\text{eq}} = \lambda_2 (1-2u)/(1+u)$, and hence, using (65),

$$\lambda_{\text{eq}} = \lambda_2 \frac{\lambda_1 + 2\lambda_2 + 2f_1(\lambda_1 - \lambda_2)}{\lambda_1 + 2\lambda_2 - f_1(\lambda_1 - \lambda_2)} \tag{66}$$

which is the exact solution of the coated-sphere problem [24] [25]. Equation (66) can be recast in a compact form that mirrors the mechanical result of Equation (38):

$$\lambda_{\text{eq}} = \lambda_2 + \frac{f_1}{\dfrac{1}{\lambda_1 - \lambda_2} + \dfrac{1-f_1}{3\lambda_2}}. \tag{67}$$

Both limiting cases are recovered: $\lambda_{\text{eq}} \to \lambda_2$ when $f_1 \to 0$ (inclusion entirely made of ITZ material) and $\lambda_{\text{eq}} \to \lambda_1$ when $f_1 \to 1$ (vanishing ITZ). The ITZ volume fraction within the coated inclusion, $1 - f_1 = 1 - (R_1/R_2)^3$, is the only geometrical parameter through which the ITZ thickness enters the thermal problem; its value is given in Section 4.1.

3.6.4. Mori-Tanaka Estimate of the Effective Conductivity

For a spherical inclusion of conductivity λ_i embedded in an infinite matrix of conductivity λ_0 subjected to a remote uniform gradient, the temperature-gradient localization tensor degenerates into the scalar

$$A_i^{\text{dil}} = \frac{3\lambda_0}{\lambda_i + 2\lambda_0}, \tag{68}$$

the thermal counterpart of the dilute strain localization tensor of Equation (12). Following the same reasoning as in Section 2.2—each inclusion sees the average gradient of the matrix rather than the macroscopic gradient—the Mori-Tanaka localization factor reads

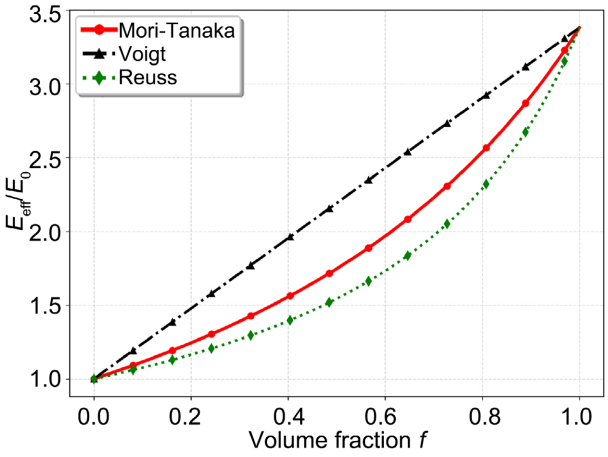
$$A_i^{\text{MT}} = \frac{A_i^{\text{dil}}}{f_0 + \sum_j f_j A_j^{\text{dil}}}, \quad f_0 = 1 - \sum_j f_j, \tag{69}$$

and the effective conductivity of a composite containing an arbitrary number of spherical inclusion families is

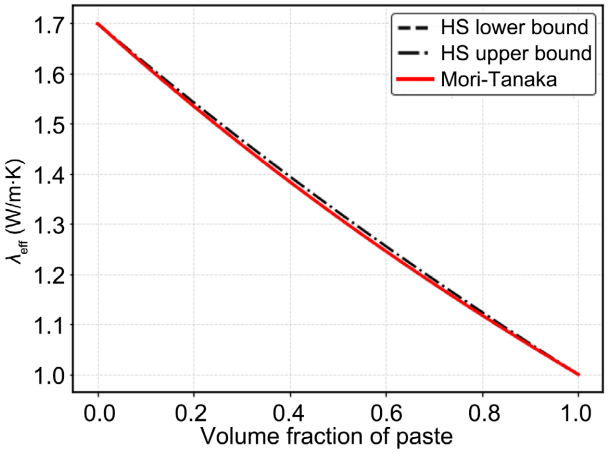
$$\lambda_{\text{eff}} = \lambda_0 + \sum_i f_i (\lambda_i - \lambda_0) A_i^{\text{MT}} \tag{70}$$

Equation (70) is the thermal analogue of Equation (19) and is the relation used to produce **Figure 7(b)**, **Figure 8(b)** and **Figure 10**.

Single family of inclusions. For one population of conductivity λ_1 and volume fraction f, (70) yields the closed form

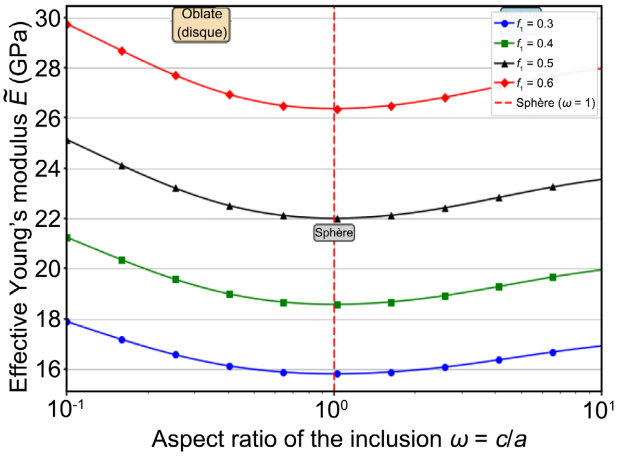


(a)

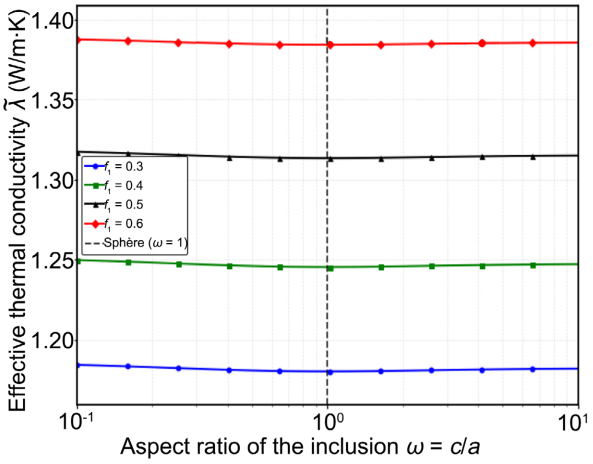


(b)

Figure 7. Verification of the micromechanical model against theoretical bounds, for the effective Young's modulus (a, computed with the matched reference value $E_1 = 35.19$ GPa, hence $E^{\text{eff}}/E_0 = 1.70$ at $f = 1$) and the effective thermal conductivity (b), as a function of the inclusion volume fraction f of the simple-inclusion system. (a) Effective young's modulus, (b) Effective thermal conductivity.



(a)



(b)

Figure 8. Evolution of the effective Young's modulus $\tilde{E}$ and of the effective thermal conductivity $\tilde{\lambda}$ as a function of the aspect ratio ω, for four inclusion volume fractions. (a) Effective Young's modulus $\tilde{E}$, (b) Effective thermal conductivity $\tilde{\lambda}$.

$$\lambda_{\text{eff}} = \lambda_0 \frac{\lambda_1 + 2\lambda_0 + 2f(\lambda_1 - \lambda_0)}{\lambda_1 + 2\lambda_0 - f(\lambda_1 - \lambda_0)} = \lambda_0 + \frac{f}{\frac{1}{\lambda_1 - \lambda_0} + \frac{1-f}{3\lambda_0}}. \tag{71}$$

Core-shell architecture. The effective conductivity is obtained by substituting $\lambda_1 \leftarrow \lambda_{\text{eq}}$ from (66) into (71), f being the outer volume fraction of coated inclusions (core + shell).

Mixed architecture. Two families are introduced in (70): bare inclusions (λ_1, fraction $f^{(s)}$) and coated inclusions (λ_{eq}, fraction $f^{(c)}$). In the study cases of Section 4 the populations are chosen so that the comparison with the two other architectures is made at equal aggregate-core content f_a.

Structural remark. Comparing (71) with the mechanical estimates (25)-(26) makes the origin of the differential sensitivity discussed in Section 6 explicit. The thermal problem involves a single stiffness-like quantity, $3\lambda_0$, whereas the mechanical problem involves two independent ones, $k_0 + \frac{4}{3}\mu_0$ for the spherical channel and $\mu_0 + \beta_0$ for the deviatoric channel. A compliant, poorly conductive ITZ degrades one denominator in the thermal case and two in the mechanical case, which is the formal statement of the argument developed in Section 6.

Bounds used for verification. The Hashin-Shtrikman bounds for a two-phase isotropic conducting composite are obtained from (71) by assigning the role of the matrix to the less conductive phase (lower bound, HS⁻) or to the more conductive one (upper bound, HS⁺):

$$\lambda^{\text{HS}\pm} = \lambda_m + \frac{f_p}{\frac{1}{\lambda_p - \lambda_m} + \frac{1-f_p}{3\lambda_m}}, \quad \begin{cases} \lambda_m = \min(\lambda_0, \lambda_1) & (\text{HS}^-) \\ \lambda_m = \max(\lambda_0, \lambda_1) & (\text{HS}^+) \end{cases} \tag{72}$$

where λ_p and f_p denote the conductivity and volume fraction of the complementary phase. It follows immediately from (71) and (72) that the Mori-Tanaka estimate coincides identically with HS⁻ whenever the continuous matrix is the less conductive phase ($\lambda_0 < \lambda_1$), which is the situation considered here [26].

4. Material Parameters and Study Cases

4.1. The Reference Case with Matched E and λ Ratios

The quantity of interest in this work is not the absolute level of either effective property but the *difference* between the two relative reductions caused by the ITZ. That difference is meaningful only if the two fields are interrogated under comparable conditions. A Mori-Tanaka estimate depends on the phase properties solely through dimensionless ratios. For the thermal problem these are λ_1/λ_0 and $\lambda_{\mathrm{ITZ}}/\lambda_0$. For the elastic problem they are the bulk- and shear-modulus ratios k_i/k_0 and μ_i/μ_0 , which are fixed by the Young's modulus and the Poisson's ratio of each phase,

$$k = \frac{E}{3(1-2\nu)}, \quad \mu = \frac{E}{2(1+\nu)}. \tag{73}$$

The reference case imposes equality of the *Young's-modulus* and *conductivity* ratios only,

$$r_{\mathrm{inc}} = \frac{E_1}{E_0} = \frac{\lambda_1}{\lambda_0}, \quad r_{\mathrm{ITZ}} = \frac{E_{\mathrm{ITZ}}}{E_0} \approx \frac{\lambda_{\mathrm{ITZ}}}{\lambda_0}, \tag{74}$$

so that the mechanical properties are derived from the thermal ones rather than taken independently from the literature: with $\lambda_1/\lambda_0 = 1.70$, the inclusion modulus is set to $E_1 = 1.70E_0 = 35.19$ GPa. Equation (74) does *not* match the elastic contrasts that actually enter the model. Because $\nu_0 = 0.23$ whereas $\nu_1 = \nu_{\mathrm{ITZ}} = 0.20$ (**Table 1**), the bulk and shear ratios differ from the thermal ones (**Table 2**): $k_1/k_0 = 1.53$ and $k_{\mathrm{ITZ}}/k_0 = 0.61$ against 1.70 and 0.70, and $\mu_1/\mu_0 = 1.74$ and $\mu_{\mathrm{ITZ}}/\mu_0 = 0.69$. The comparison between δE and $\delta\lambda$ below is therefore *conditional on the selected Poisson's ratios*, and its intrinsic part cannot be attributed to the structure of the two problems alone.

Table 1. Properties of the mortar phases.

Phase	E (GPa)	ν	λ (W·m⁻¹·K⁻¹)	Reference	Reference case (matched E , λ ratios)
Cement paste (matrix)	20.7	0.23	1.0	28 days [27] [28]	$E_0 = 20.7$, $\nu_0 = 0.23$, $\lambda_0 = 1.0$
Silica sand	70.0	0.20 - 0.25	1.7 - 2.5	[29]	$E_1 = 35.19$, $\nu_1 = 0.20$, $\lambda_1 = 1.7$
ITZ	13.8 - 15.0	0.20 - 0.25	0.7	[27] [30]; λ adopted	$E_{\mathrm{ITZ}} = 14$, $\nu_{\mathrm{ITZ}} = 0.20$, $\lambda_{\mathrm{ITZ}} = 0.7$

E : Young's modulus; ν : Poisson's ratio; λ : thermal conductivity. The value $E_1 = 35.19$ GPa is not a measured property of quartz; it is the mechanical counterpart of $\lambda_1/\lambda_0 = 1.70$ under the matching condition (74).

Table 2. Inclusion-to-matrix and ITZ-to-matrix property ratios of the reference case. Only the E and λ columns are matched by construction; the k and μ columns follow from Equation (73) and the Poisson's ratios of Table 1.

Ratio to the matrix	E	k	μ	λ
Inclusion ($i=1$)	1.70	1.53	1.74	1.70
ITZ	0.68	0.61	0.69	0.70

Table 1 lists the literature ranges for the phases of the mortar considered, which motivate the choice of E_0, λ_0, λ_1 and the ITZ properties, together with the values adopted in the reference case. The effect of relaxing the matching condition, and of restoring the much higher stiffness contrast of quartz aggregates, is quantified separately in Section 5.5.

The resulting Young's-modulus and conductivity ratios are $r_{\text{inc}}=1.70$ for both fields, and $E_{\text{ITZ}}/E_0=0.68$ against $\lambda_{\text{ITZ}}/\lambda_0=0.70$, *i.e.* matched to within 3%. Table 2 reports all the ratios entering the two problems.

Provenance and conditioning of the adopted properties. No specific mix is modelled: the cement-paste values ($E_0=20.7$ GPa, $\nu_0=0.23$, $\lambda_0=1.0$ W·m^{-1}·K^{-1}) describe an indicative paste cured for 28 days, and the model prescribes no water-to-cement ratio, porosity or curing regime. These properties depend on the water-to-cement ratio, the capillary porosity, the curing state (age, temperature and moisture) and the mix composition (binder type, admixtures), so that the reference case is representative of a generic paste rather than of a specific mortar. The elastic moduli of hardened pastes vary markedly with the water-to-cement ratio and the degree of hydration [31]; the value adopted for E_0 lies in the range of 20 - 22 GPa obtained for the cement matrix of mortars by nanoindentation-based homogenization [27]. The Poisson's ratio varies only between about 0.21 and 0.23 over the usual range of water-to-cement ratios [32], consistently with the values adopted here. A thermal conductivity of 1 W·m^{-1}·K^{-1} is commonly quoted for hydrated pastes with water-to-cement ratios of 0.3 - 0.4, within a reported range of 0.53 to 1.16 W·m^{-1}·K^{-1} [28]. The conductivity decreases with increasing porosity and water-to-cement ratio and depends on the degree of saturation and on the curing regime (sealed or saturated) [33] [34]. The modulus of the siliceous aggregate (70 GPa) is the value commonly used for sand in meso-scale mortar models [35].

The ITZ is a layer that is softer, more porous and less conductive than the bulk paste [5] [6]. The adopted modulus ($E_{\text{ITZ}}=13.8$ - 15.0 GPa) lies within the range of nanoindentation values reported for the ITZ of mortars (average of 14.8 GPa, individual values from 11 to 28 GPa) [27]. It corresponds to 0.67 - 0.72 of E_0, *i.e.* at or slightly below the lower bound of the 70% - 85% of the paste modulus reported for the ITZ [30], with a ratio that depends on the water-to-cement ratio [36]. The ITZ conductivity ($\lambda_{\text{ITZ}}=0.7$ W·m^{-1}·K^{-1}) is a value adopted by the authors: no measured value was found in the literature, and the ratio $\lambda_{\text{ITZ}}/\lambda_0=0.70$ reflects the higher porosity of the ITZ and is used to set the matched contrast of Equation (74). The sensitivity of the results to E_{ITZ} is illustrated in Section 5.5.

The real ITZ contains a gradient of porosity and properties. Following the classical approach of replacing this gradient by a single shell of uniform properties [37], the ITZ enters the model only through the ratio R_1/R_2, so that $R_1/R_2 = 0.9$ corresponds to a thickness of $0.1R_2$. For comparison, a mean ITZ thickness of 48.3 μm was derived from elastic wave speeds in a mortar made of 20 - 30 screened sand with a water-to-cement ratio of 0.3 [38], and 20 μm was measured in a mortar at 88 days [27]. The Mori-Tanaka scheme has no characteristic length, so no aggregate radius is prescribed and $R_1/R_2 = 0.9$ is a dimensionless geometric choice. For an ITZ thickness of 20 - 50 μm, it corresponds to an aggregate radius of 0.2 - 0.5 mm, *i.e.* a fine sand. Because porosity, curing and mix composition shift the adopted elastic and thermal contrasts, the reference case should be read as a controlled numerical configuration, not as a direct representation of a particular mortar.

The geometry of the coated inclusion is fixed by the ratio R_1/R_2, from which the ITZ volume fraction within the inclusion follows as $1-\left(R_1/R_2\right)^3$. In all computations reported below, $R_1/R_2 = 0.9$, corresponding to an ITZ occupying 27.1% of the volume of the coated inclusion.

Volume-fraction convention. All architectures are compared at the same *aggregate-core* volume fraction f_a, *i.e.* the same volume of aggregate per unit volume of composite, and the ITZ fraction is reported separately. Holding instead the outer coated-particle fraction constant would replace part of the reference aggregate volume with ITZ material, so that the reported reduction would combine an ITZ effect with a lower aggregate content. With $c = R_1/R_2 = 0.9$ (so $c^3 = 0.729$), the three architectures are defined as follows.

- *Single inclusions* (*reference*, *no ITZ*): bare aggregates of fraction f_a in the paste.
- *Core-shell*: all aggregates are coated. The outer coated-particle fraction is $f^{(c)} = f_a/c^3$, the ITZ fraction is $f_{ITZ} = f_a\left(c^{-3}-1\right) \approx 0.372\, f_a$, and the paste fraction is $1- f_a/c^3$.
- *Mixed*: the aggregate content is split equally between the two populations, *i.e.* bare aggregates $f^{(s)} = f_a/2$ and coated aggregates whose core fraction is $f_a/2$, hence $f^{(c)} = f_a/\left(2c^3\right)$ and $f_{ITZ} = f_a\left(c^{-3}-1\right)/2$.

In the notation of Section 3, f is the outer volume fraction of the inclusions of each family, so that $f = f_a$ for bare inclusions and $f = f^{(c)}$ for coated ones. The resulting fractions are listed in **Table 3**. At $f_a = 0.6$ the core-shell system has an outer coated fraction of 0.82 and a paste fraction of only 0.18, which bears on the validity of the Mori-Tanaka estimate (Section 7).

Table 3. Volume fractions of the architectures at fixed aggregate-core fraction f_a ($R_1/R_2 = 0.9$).

f_a	Core-shell			Mixed		
	$f^{(c)}$	f_{ITZ}	paste	$f^{(s)} + f^{(c)}$	f_{ITZ}	paste
0.2	0.274	0.074	0.726	0.237	0.037	0.763

Continued

0.4	0.549	0.149	0.451	0.474	0.074	0.526
0.6	0.823	0.223	0.177	0.711	0.111	0.289

4.2. Investigated Configurations

Three microstructural configurations are examined: an RVE composed of simple spherical inclusions, an RVE with coated inclusions and interphase, and a mixed RVE combining these two populations in a single matrix. Each configuration is computed with the Python Echoes library [39].

5. Results

5.1. Model Consistency

As **Figure 7** shows, the hierarchical ordering of the computed effective properties, bracketed by the Voigt and Reuss bounds, is consistent with the classical results of continuum micromechanics [4] [20] for the effective Young's modulus. Panel (a) is computed with the matched reference value $E_1 = 35.19$ GPa of **Table 1** ($E_1/E_0 = 1.70$), so that E^{eff}/E_0 tends to 1.70 at $f = 1$, the same limit as the conductivity ratio in panel (b). Because $k_1 > k_0$ and $\mu_1 > \mu_0$, the Mori-Tanaka estimate of the simple elastic case coincides with the lower Hashin-Shtrikman bound. Furthermore, the thermal conductivity predicted by the Mori-Tanaka scheme coincides with the lower Hashin-Shtrikman bound (HS^-), as required analytically by Equations (71)-(72). This agreement is well established for isotropic two-phase composites when the inclusions are spherical and embedded in a less conductive continuous matrix ($\lambda_0 < \lambda_1$) [4] [20] [26]. At the moderate contrast of the reference case, the two Hashin-Shtrikman bounds are close to each other, so the agreement in **Figure 7(b)** is a necessary but weak test; it becomes discriminating only at higher contrast. Moreover, this consistency concerns the simple (uncoated) case only. It verifies the implementation, but it does not establish predictive accuracy for densely packed coated or mixed architectures, for which the results of Section 5 are Mori-Tanaka estimates for a continuous matrix (Section 7).

5.2. Effect of Inclusion Shape

The results of Sections 5.3 - 5.5 are obtained for spherical inclusions. Before turning to the ITZ, we quantify how far this idealisation influences the predicted effective properties. The inclusions are modelled as spheroids of revolution with equatorial semi-axis a and symmetry semi-axis c, characterised by the aspect ratio

$$\omega = \frac{c}{a}, \tag{75}$$

so that three regimes are covered:

- *Oblate* spheroids ($\omega < 1$, $c < a$), representing disk- or flake-like particles;
- *Spheres* ($\omega = 1$, $c = a$);

- *Prolate* spheroids ($\omega > 1$, $c > a$), representing elongated fibre- or needle-like particles.

The inclusions are assumed to be randomly oriented with a uniform orientation distribution, so that the homogenised medium remains macroscopically isotropic and the effective properties can still be described by the two scalars $\tilde{E}$ and $\tilde{\lambda}$. The configuration plotted in **Figure 8** is the simple-inclusion system, and all material parameters are those of **Table 1**.

Shape-dependent localization. For the thermal problem, the localization factor of a spheroid along its principal direction i is governed by the depolarization factors N_i, which satisfy $N_1 + N_2 + N_3 = 1$ and, for a spheroid, $N_1 = N_2 = (1 - N_3)/2$ with

$$N_3 = \begin{cases} \dfrac{1}{1-\omega^2}\left[1 - \dfrac{\omega}{\sqrt{1-\omega^2}}\arcsin\sqrt{1-\omega^2}\right], & \omega < 1 \quad (\text{oblate}), \\ \dfrac{1-e^2}{e^2}\left[\dfrac{1}{2e}\ln\dfrac{1+e}{1-e} - 1\right], e = \sqrt{1-\omega^{-2}}, & \omega > 1 \quad (\text{prolate}), \end{cases} \tag{76}$$

both branches tending to $N_3 = 1/3$ as $\omega \to 1$. The dilute localization factor along direction i is then

$$A_i^{\text{dil}}(\omega) = \frac{\lambda_0}{\lambda_0 + N_i(\omega)(\lambda_1 - \lambda_0)}, \tag{77}$$

and its orientation average $\langle A^{\text{dil}} \rangle = \frac{1}{3}\sum_i A_i^{\text{dil}}$ is substituted into (69)-(70). For the elastic problem, the corresponding Eshelby tensor of a spheroid embedded in an isotropic matrix depends on ω and ν_0; its components are given in closed form by Mura [22] and are reproduced in Appendix A. The orientation average of $\mathbb{A}^{\text{dil}}$ is performed before the Mori-Tanaka normalisation, following Benveniste [20].

Results. **Figure 8** shows $\tilde{E}$ and $\tilde{\lambda}$ as functions of ω for four inclusion volume fractions. For every volume fraction, both properties reach a *global minimum* at $\omega = 1$: any departure from sphericity, whether oblate or prolate, increases the effective stiffness and the effective conductivity. At the moderate contrast of the reference case the amplitude of this effect is small—at $f = 0.6$, going from $\omega = 1$ to $\omega = 10$ raises $\tilde{\lambda}$ by only 0.2%, and $\tilde{E}$ by 6.3%—and it saturates beyond $\omega \approx 10$. The effect would be substantially larger for stiffer or more conductive inclusions, since the shape dependence enters (77) only through the product $N_i(\lambda_1 - \lambda_0)$.

This minimum is not a numerical accident: for the conduction problem it can be established exactly. Since A_i^{dil} in (77) is a convex function of N_i, Jensen's inequality applied to the orientation average, together with the constraint $\sum_i N_i = 1$, gives

$$\left\langle A^{\text{dil}}(\omega) \right\rangle = \frac{1}{3}\sum_i \frac{\lambda_0}{\lambda_0 + N_i \Delta\lambda} \geq \frac{\lambda_0}{\lambda_0 + \frac{1}{3}\Delta\lambda} = \left\langle A^{\text{dil}}(1) \right\rangle, \quad \Delta\lambda = \lambda_1 - \lambda_0, \tag{78}$$

with equality if and only if $N_1 = N_2 = N_3 = 1/3$, *i.e.* for the sphere. Since λ_{eff} is an increasing function of $\langle A^{\text{dil}} \rangle$ when $\lambda_1 > \lambda_0$, the sphere minimises the effective conductivity among all randomly oriented spheroids at fixed volume fraction. Physically, the sphere is the only shape whose depolarization factor is simultaneously maximal in all three directions: it is the geometry for which the inclusion is most efficiently screened by the surrounding matrix. Any elongation or flattening lowers the depolarization factor along one direction— $N_3 \to 0$ for a needle, $N_1 = N_2 \to 0$ for a disk—so that the inclusion carries an increasingly larger share of the flux along that direction, and the orientation average is dominated by this most favourable orientation. The same screening argument transposes qualitatively to elasticity, where the components of the Eshelby tensor play the role of the depolarization factors, and accounts for the identical shape of the two panels of Figure 8.

It is worth noting that the ordering is reversed for inclusions *less* conductive or *more* compliant than the matrix, for which the sphere maximises the effective property; the minimum reported here is therefore specific to the stiff, conductive aggregates considered in this work.

Two consequences follow for the remainder of the study. First, the spherical idealisation adopted in Sections 5.3 - 5.5 is *conservative*: it yields the lowest effective properties among spheroidal morphologies, so the ITZ-induced losses reported below are not artefacts of an over-optimistic geometry. Second, since both properties respond to shape in the same direction and with comparable relative amplitude, the differential indicator $\delta E - \delta\lambda$ introduced in Section 5.5 is largely insensitive to the morphological assumption, which strengthens the generality of the conclusion drawn there.

Caveat. For non-spherical inclusions the orientation-averaged Mori-Tanaka estimate is known to lose the diagonal symmetry of the effective stiffness tensor in the general multi-phase case [40]. This restriction does not affect Sections 5.3 - 5.5: the same authors show that two-phase systems, and multi-phase systems whose typical inclusion is a coated particle, retain diagonal symmetry. The caveat therefore concerns only the randomly oriented spheroids of the present section, whose results should not be extrapolated to strongly anisotropic or highly concentrated systems without further verification.

5.3. Effective Young's Modulus: Effect of Inclusion Configuration

Figure 9 shows the normalized effective Young's modulus E^{eff}/E_0 predicted by the Mori-Tanaka scheme as a function of the aggregate-core volume fraction f_a, over $0 \le f_a \le 0.6$. As expected, introducing stiffer aggregates ($E_1 = 35.19$ GPa) into the cementitious matrix ($E_0 = 20.7$ GPa) increases the overall stiffness. However, the presence of a compliant ITZ ($E_{\text{ITZ}} = 14$ GPa), which replaces part of the paste at fixed aggregate content, attenuates this reinforcement. At $f_a = 0.6$, the normalized modulus reaches 1.37 for the ideal single-inclusion case, against 1.24 for the fully ITZ-affected core-shell microstructure, whose ITZ fraction is 0.22 (Table 3), and 1.30 for the mixed system.

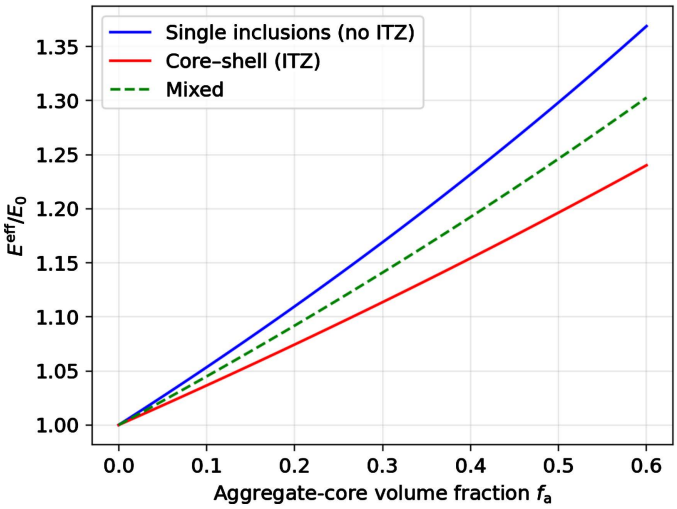


Figure 9. Effect of the inclusion configuration on the effective Young's modulus, at fixed aggregate-core volume fraction f_a.

5.4. Effective Thermal Conductivity: Effect of Inclusion Configuration

Figure 10 shows the normalized effective thermal conductivity λ_{eff}/λ_0 predicted by the Mori-Tanaka scheme as a function of the aggregate-core volume fraction f_a ($0 \le f_a \le 0.6$). As expected, incorporating conductive aggregates ($\lambda_1 = 1.70$ $W \cdot m^{-1} \cdot K^{-1}$) into the cementitious matrix ($\lambda_0 = 1.00$ $W \cdot m^{-1} \cdot K^{-1}$) enhances the overall heat conduction. The porous, lower-conductivity ITZ ($\lambda_{ITZ} = 0.70$ $W \cdot m^{-1} \cdot K^{-1}$) acts as a thermal barrier and reduces this enhancement. At $f_a = 0.6$, the normalized conductivity reaches 1.38 for the ideal single-inclusion system, whereas it falls to 1.28 for the fully ITZ-affected core-shell microstructure and to 1.33 for the mixed system. Whether this reduction is a loss or a benefit depends on the thermal objective (Section 5.5).

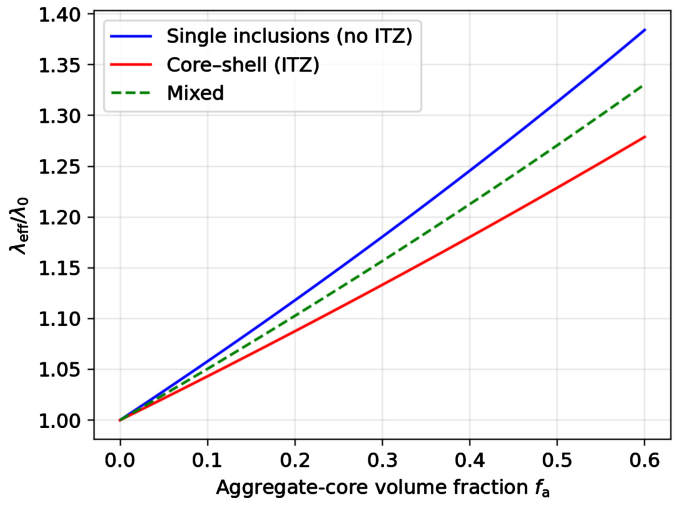


Figure 10. Effect of the inclusion configuration on the effective thermal conductivity, at fixed aggregate-core volume fraction f_a.

5.5. Comparative Thermo-Mechanical Analysis

This section addresses directly the central question raised in the Introduction: does the presence of a compliant, poorly conductive ITZ reduce the effective Young's modulus and the effective thermal conductivity to the same extent?

Indicators and thermal objective. To quantify the ITZ effect, a relative reduction indicator is defined for each property P ($P = E$ or λ), computed with respect to the ideal single-inclusion system (no ITZ) taken as reference at the same aggregate-core volume fraction f_a:

$$\delta P(f_a) = \frac{P_{\text{ideal}}(f_a) - P_{\text{ITZ}}(f_a)}{P_{\text{ideal}}(f_a)} \tag{79}$$

where P_{ITZ} denotes either the fully ITZ-affected core-shell configuration or the mixed configuration. Since the aggregate content is the same in both terms, δP isolates the effect of the ITZ replacing part of the paste, and the ITZ fraction is reported separately (Table 3).

The meaning of δP depends on the thermal objective, which must be stated. The stiffness reduction δE is a loss whatever the application. For thermal conductivity, two objectives are possible: a high conductivity (heat dissipation or transfer), for which a reduction is a loss, or thermal insulation, for which a reduction is beneficial. In the present case the aggregates are more conductive than the paste ($\lambda_1/\lambda_0 = 1.70$) and the ITZ is less conductive ($\lambda_{\text{ITZ}}/\lambda_0 = 0.70$), so the ITZ lowers λ_{eff} with respect to the ITZ-free reference. For an insulating concrete this is a benefit. $\delta\lambda$ is therefore reported as a *conductivity reduction* and not as a performance loss; only the sign of the objective decides how it is read. The ratio $\delta E/\delta\lambda$ then measures the stiffness lost per unit of conductivity reduction.

Because the two fields are probed at matched E and λ ratios (Section 4.1), the difference between δE and $\delta\lambda$ does not stem from the choice of the Young's-modulus and conductivity contrasts. It remains conditional on the Poisson's ratios, which set the bulk- and shear-modulus ratios (Table 2), and on the 3% residual mismatch of the ITZ ratio.

As Figure 11 shows, at $f_a = 0.6$ the fully ITZ-affected core-shell microstructure induces a stiffness reduction of $\delta E \approx 9.4\%$, compared with a conductivity reduction of $\delta\lambda \approx 7.6\%$ ($\delta E/\delta\lambda \approx 1.24$). The stiffness reduction exceeds the conductivity reduction over the whole range $0.1 \le f_a \le 0.6$ investigated, and the gap widens steadily with f_a, from 0.2 percentage points at $f_a = 0.1$ to 1.1 at 0.4 and 1.8 at 0.6.

As Figure 12 shows, the mixed inclusion system reduces both quantities to $\delta E \approx 4.8\%$ and $\delta\lambda \approx 3.9\%$ at $f_a = 0.6$—about one half of the core-shell values, at equal aggregate content—while preserving the same ordering, with a residual gap of 1.0 percentage point.

Sensitivity to the matching condition. The gap is small in absolute terms and sensitive to the inputs. Setting $E_{\text{ITZ}} = 14.49$ GPa, which matches the ITZ ratio exactly (0.70), lowers δE to 8.5% at $f_a = 0.6$ and the gap to 0.9 points. Taking

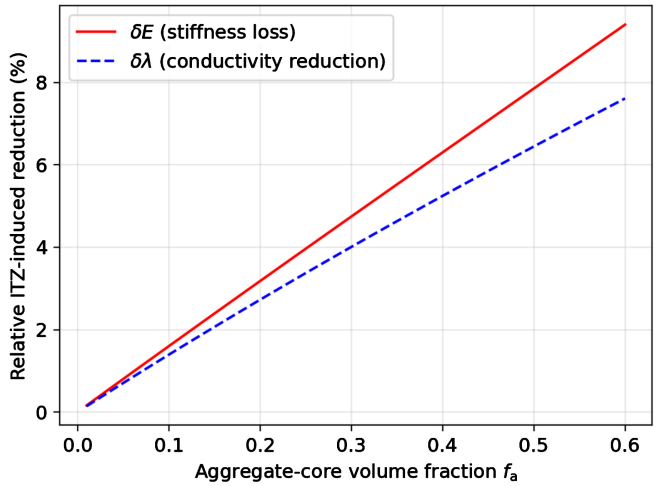


Figure 11. Relative ITZ-induced stiffness loss (δE) and conductivity reduction ($\delta\lambda$), as a function of the aggregate-core volume fraction f_a, for the fully ITZ-affected core-shell system.

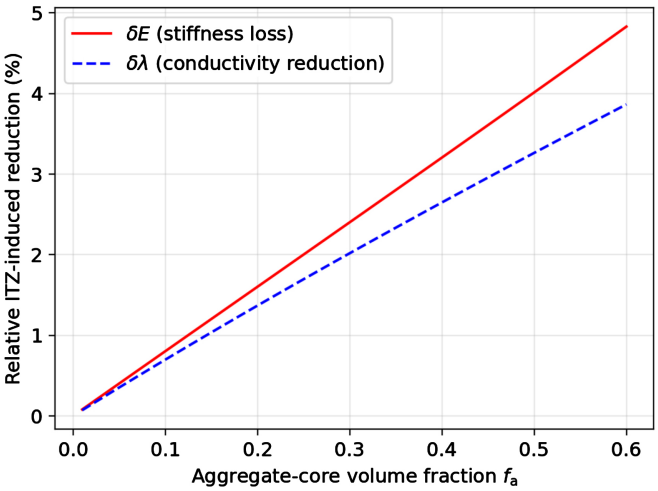


Figure 12. Relative ITZ-induced stiffness loss (δE) and conductivity reduction ($\delta\lambda$), as a function of the aggregate-core volume fraction f_a, for the mixed inclusion system.

in addition $\nu = 0.23$ for all phases, so that the E, k and μ ratios all coincide with the conductivity ratios, leaves the gap at 0.9 points. In this configuration the Poisson's-ratio mismatch of the reference case contributes about 0.03 points, and the residual 3% mismatch of the ITZ stiffness ratio about 0.85 points. Roughly half of the 1.8-point gap of the reference case thus reflects unmatched inputs, and the asymmetry at fully matched ratios is of the order of one percentage point.

Effect of the contrast level. The matched-ratio construction limits the bias due to the contrast level, but it does not describe a real mortar, in which the stiffness contrast of quartz aggregates greatly exceeds their thermal contrast. Repeating the computation with $E_1 = 70$ GPa ($r_{inc} = 3.38$ mechanically, against 1.70 thermally) raises δE to 11.4% at $f_a = 0.6$, while $\delta\lambda$ is unchanged at 7.6%, so that the gap widens from 1.8 to 3.8 percentage points. The contrast level therefore

roughly doubles the asymmetry: in realistic mortars a substantial part of the observed difference between the two reductions originates in the disparity of the property contrasts, the rest in the structure of the two problems and in the residual input mismatch discussed above. Distinguishing the contributions is what the matched comparison makes possible.

Validity at high inclusion content. At $f_a = 0.6$ the core-shell system has an outer coated fraction of 0.82 and a paste fraction of 0.18 (the mixed system 0.71 and 0.29). The results at high inclusion content are Mori-Tanaka estimates for a continuous matrix. The Hashin-Shtrikman consistency of the simple thermal case (Section 5.1) does not establish predictive accuracy for densely packed coated or mixed architectures, and the high-content values should be read as trends. The conclusions drawn from the sign and the order of magnitude of the gap hold from $f_a \approx 0.2$, where the outer fraction is 0.27.

The physical origin of the intrinsic part of this differential sensitivity, and its practical implications for cementitious composite design, are examined in Section 6.

6. Discussion

The results presented in Section 5.5 show that, at matched Young's-modulus and conductivity ratios, the interfacial transition zone does not reduce the mechanical and thermal responses of the composite to the same extent: the stiffness loss exceeds the conductivity reduction, by 1.8 percentage points at $f_a = 0.6$ for the core-shell architecture and by 1.0 point for the mixed one. The asymmetry is systematic in sign but modest in magnitude. It is conditional on the selected Poisson's ratios and sensitive to the residual input mismatch (it falls to about 0.9 point at fully matched ratios), and it should not be confused with the larger gaps obtained when the two fields are probed at different contrasts.

Physical interpretation. This differential sensitivity can be related to the tensorial nature of the two problems, and the analytical form of the estimates makes the argument explicit. The stiffness tensor couples the spherical (k) and deviatoric (μ) components of strain through two distinct projectors ($\mathbb{J}$ and $\mathbb{K}$, Equations (3)-(4)), and the two Mori-Tanaka estimates (25)-(26) involve two independent denominators, $k_0 + \frac{4}{3}\mu_0$ and $\mu_0 + \beta_0$, the latter being highly sensitive to the ratio $\mu_{\mathrm{ITZ}}/\mu_{\mathrm{matrix}}$ through Equation (27). Thermal conduction, by contrast, is a scalar single-channel transport problem: the corresponding estimate (71) involves the single quantity $3\lambda_0$, with no spherical/deviatoric decomposition. A compliant, poorly conductive ITZ therefore degrades two load-transfer channels in the mechanical case against a single transport channel in the thermal case. The same asymmetry appears geometrically in the shape analysis of Section 5.2, where conduction is governed by a single scalar N_i whereas elasticity requires a fourth-order tensor with two independent invariants (Appendix A.2). This is consistent with a slightly higher sensitivity of stress transfer across the aggregate-matrix interface to interfacial softness than of conductive flux to interfacial resistance.

Given the small size of the gap and its sensitivity to the inputs, this is a plausible mechanism rather than a demonstrated one.

Design implications. From a material design standpoint, three conclusions follow. First, at matched ratios the asymmetry attached to the mechanical field is small: selecting aggregates for stiffness does not carry a disproportionate thermal cost. Second, the amplification measured in Section 5.5 shows that in real mortars the mechanical reduction associated with the ITZ is governed to a large extent by the stiffness contrast of the aggregate. Strategies aimed at stiffening the composite through high-modulus aggregates therefore incur an ITZ-related loss that grows with that contrast, whereas the thermal side is unchanged. Third, the reading of $\delta\lambda$ depends on the thermal objective: for an insulating concrete the ITZ-induced conductivity reduction is a benefit, so the ITZ trades a stiffness loss against a gain in insulation, whereas for conduction-driven applications it is a loss for both properties.

The mixed architecture as a design lever. The mixed inclusion system offers a practical route to mitigate this trade-off: combining a population that develops a significant ITZ with a population for which the ITZ contribution is comparatively negligible roughly halves both ITZ-induced reductions (stiffness loss from 9.4% to 4.8%, conductivity reduction from 7.6% to 3.9%) at constant aggregate-core fraction. For an insulating application this recovers about half of the stiffness lost to the ITZ while giving up about half of the ITZ-induced conductivity reduction.

This suggests that the ITZ volume fraction per inclusion, rather than the total inclusion content alone, is an underexploited design variable in ITZ-aware composite formulation, and demonstrates the value of coupled thermo-mechanical homogenization for optimizing sustainable cementitious composites.

Toward a design map. The proposed differential sensitivity indicator, $\delta E - \delta\lambda$, could be mapped over the full parameter space (volume fraction, ITZ property contrast, ITZ thickness, and the ratio between the mechanical and thermal contrasts) to identify the region where the mechanical-thermal trade-off is most pronounced and, conversely, the region where it is minimized. The two computations reported in Section 5.5 are two points of that map.

7. Limitations

Several limitations should be acknowledged. The reference case is built on matched Young's-modulus and conductivity ratios, which is what makes the comparison meaningful but which also means that the adopted E_1 is not the modulus of a real siliceous aggregate; the realistic case is treated only as a single complementary computation. The matching holds for the Young's-modulus and conductivity ratios only: the bulk- and shear-modulus ratios depend on the adopted Poisson's ratios, and a 3% mismatch remains on the ITZ ratio, so the reported gap is conditional on these inputs. The phase properties are adopted values, and their dependence on porosity, curing state and mix composition has not been calibrated on a specific mortar. At high inclusion content (outer coated fraction up to 0.82

at $f_a = 0.6$), the results are Mori-Tanaka estimates for a continuous matrix; the Hashin-Shtrikman consistency of the simple thermal case does not establish predictive accuracy for densely packed coated or mixed architectures. The ITZ is modelled with uniform thickness and constant properties across all inclusions, whereas real mortars exhibit ITZ characteristics that vary with aggregate size and mineralogy. The inclusion shapes considered (spherical, and spheroidal in Section 5.2) do not capture the full morphological complexity of real aggregates. Cross-coupling between the mechanical and thermal fields—notably differential thermal expansion between phases—is not addressed, and could in principle modify the differential sensitivity reported here under non-isothermal loading conditions. Finally, the comparison with experimental data remains limited; future work should combine the present analytical framework with experimental measurements on mortars of controlled aggregate volume fraction and ITZ characteristics, in order to assess the predictive capability of the model.

8. Conclusions

This work proposed a unified micromechanical framework, based on Eshelby's equivalent inclusion theory and the Mori-Tanaka homogenization scheme extended to coated inclusions via the Hervé-Zaoui model, to jointly compute the effective Young's modulus and the effective thermal conductivity of cementitious composites under a common inclusion architecture, at matched Young's-modulus and conductivity ratios and at fixed aggregate-core volume fraction.

The central question posed in the Introduction—whether the interfacial transition zone reduces both effective properties to the same extent—was answered in the negative. For the fully ITZ-affected system, the relative stiffness loss ($\delta E \approx 9.4\%$ at $f_a = 0.6$) exceeds the relative conductivity reduction ($\delta\lambda \approx 7.6\%$) across the investigated range. The gap is small, 1.8 percentage points, and conditional on the selected Poisson's ratios and on the residual mismatch of the ITZ ratio: it falls to about 0.9 point at fully matched ratios. It is consistent with the two-channel (spherical and deviatoric) nature of mechanical load transfer as opposed to the single-channel nature of thermal transport. Restoring the realistic stiffness contrast of quartz aggregates widens the gap to 3.8 percentage points, which shows that a substantial part of the asymmetry observed in real mortars comes from the disparity of the property contrasts rather than from the structure of the two problems. Whether the conductivity reduction is a loss or a benefit depends on the thermal objective: it is beneficial for insulating concretes.

The mixed inclusion system, combining bare and fully coated aggregates, reduces both quantities to $\delta E \approx 4.8\%$ and $\delta\lambda \approx 3.9\%$ at $f_a = 0.6$, indicating that the ITZ volume fraction per inclusion, at fixed aggregate content, is a design lever for balancing structural stiffness against thermal insulation. These results at high inclusion content are Mori-Tanaka estimates for a continuous matrix and are not validated against dense coated or mixed packings.

This framework requires only a limited set of input parameters (elastic modulus,

thermal conductivity, Poisson's ratio, and phase volume fractions), making it directly applicable to the rapid evaluation and optimization of cementitious composite formulations. Future work should extend the ITZ representation to variable thickness, incorporate cross-field thermo-mechanical coupling, map the differential indicator over the joint contrast space, and confront the model with a systematic experimental dataset in order to generalize the $\delta E/\delta\lambda$ ratio identified here.

Author Contributions

Koffi Apélété Konde and Komi Apélété Amou conceptualized the study, developed the micromechanical homogenization framework, implemented the numerical simulations, performed the formal analysis, and wrote the original draft. Kossi Tepe contributed to the conceptualization of the study, validated the analytical models, supervised the research work, and critically reviewed and edited the manuscript. All authors read and approved the final version of the manuscript.

Conflicts of Interest

The authors declare no conflicts of interest regarding the publication of this paper.

References

[1] Wu, C., Liu, S.Q., Guo, J.P., Ma, H.Q. and He, L. (2023) Relationship between Thermal Conductivity and Compressive Strength of Insulation Concrete: A Review. *Journal of Research Updates in Polymer Science*, **12**, 80-96. https://doi.org/10.6000/1929-5995.2023.12.08

[2] Remesar, J.C., Vera, S. and Lopez, M. (2017) Assessing and Understanding the Interaction between Mechanical and Thermal Properties in Concrete for Developing a Structural and Insulating Material. *Construction and Building Materials*, **132**, 353-364. https://doi.org/10.1016/j.conbuildmat.2016.11.116

[3] Torquato, S. (2002) Random Heterogeneous Materials: Microstructure and Macroscopic Properties, Volume 16. Springer.

[4] Zaoui, A. (2002) Continuum Micromechanics: Survey. *Journal of Engineering Mechanics*, **128**, 808-816. https://doi.org/10.1061/(asce)0733-9399(2002)128:8(808)

[5] Scrivener, K.L., Crumbie, A.K. and Laugesen, P. (2004) The Interfacial Transition Zone (ITZ) between Cement Paste and Aggregate in Concrete. *Interface Science*, **12**, 411-421. https://doi.org/10.1023/b:ints.0000042339.92990.4c

[6] Zheng, J.J., Li, C.Q. and Zhou, X.Z. (2005) Thickness of Interfacial Transition Zone and Cement Content Profiles around Aggregates. *Magazine of Concrete Research*, **57**, 397-406. https://doi.org/10.1680/macr.2005.57.7.397

[7] Chung, S.Y. and Kim, J.S. (2024) Investigation of Gradient Properties for Cement Mortar Interfacial Transition Zones and Their Effects on Mechanical Characteristics Using Micro-CT. *Developments in the Built Environment*, **18**, Article ID: 100390. https://doi.org/10.1016/j.dibe.2024.100390

[8] Chen, Q.Q., Zhang, J., Wang, Z.Y., Zhao, T.T. and Wang, Z.H. (2024) A Review of the Interfacial Transition Zones in Concrete: Identification, Physical Characteristics, and Mechanical Properties. *Engineering Fracture Mechanics*, **300**, Article ID: 109979. https://doi.org/10.1016/j.engfracmech.2024.109979

[9] Hashin, Z., *et al.* (1960) The Elastic Moduli of Heterogeneous Materials, Volume 9. US Department of Commerce, Office of Technical Services.

[10] Eshelby, J.D. (1957) The Determination of the Elastic Field of an Ellipsoidal Inclusion, and Related Problems. *Proceedings of the Royal Society of London. Series A. Mathematical and Physical Sciences*, **241**, 376-396. https://doi.org/10.1098/rspa.1957.0133

[11] Mori, T. and Tanaka, K. (1973) Average Stress in Matrix and Average Elastic Energy of Materials with Misfitting Inclusions. *Acta Metallurgica*, **21**, 571-574. https://doi.org/10.1016/0001-6160(73)90064-3

[12] Christensen, R.M. and Lo, K.H. (1979) Solutions for Effective Shear Properties in Three Phase Sphere and Cylinder Models. *Journal of the Mechanics and Physics of Solids*, **27**, 315-330. https://doi.org/10.1016/0022-5096(79)90032-2

[13] Bohm, H. and Nogales, S. (2008) Mori-Tanaka Models for the Thermal Conductivity of Composites with Interfacial Resistance and Particle Size Distributions. *Composites Science and Technology*, **68**, 1181-1187. https://doi.org/10.1016/j.compscitech.2007.06.009

[14] Liu, Q., Jin, C. and Li, X. (2024) Impact of Interfacial Transition Zone on Concrete Mechanical Properties: A Comparative Analysis of Multiphase Inclusion Theory and Numerical Simulations. *Coatings*, **14**, Article 698. https://doi.org/10.3390/coatings14060698

[15] Xu, W.X., Fu, J.L., Hua, R.Y. and Han, F.Y. (2024) ITZ Volume Fraction and Thermal Conductivity of Concrete: A Unified Random Packing Model for Gravels and Crushed Rocks. *Journal of Building Engineering*, **90**, Article ID: 109457. https://doi.org/10.1016/j.jobe.2024.109457

[16] Herve, E. and Zaoui, A. (1993) Inclusion-Based Micromechanical Modelling. *International Journal of Engineering Science*, **31**, 1-10. https://doi.org/10.1016/0020-7225(93)90059-4

[17] Geers, M.G.D., Kouznetsova, V.G. and Brekelmans, W.A.M. (2010) Multi-Scale Computational Homogenization: Trends and Challenges. *Journal of Computational and Applied Mathematics*, **234**, 2175-2182. https://doi.org/10.1016/j.cam.2009.08.077

[18] Hill, R. (1963) Elastic Properties of Reinforced Solids: Some Theoretical Principles. *Journal of the Mechanics and Physics of Solids*, **11**, 357-372. https://doi.org/10.1016/0022-5096(63)90036-x

[19] Tokovyy, Y. and Ma, C. (2019) Elastic Analysis of Inhomogeneous Solids: History and Development in Brief. *Journal of Mechanics*, **35**, 613-626. https://doi.org/10.1017/jmech.2018.57

[20] Benveniste, Y. (1987) A New Approach to the Application of Mori-Tanaka's Theory in Composite Materials. *Mechanics of Materials*, **6**, 147-157. https://doi.org/10.1016/0167-6636(87)90005-6

[21] Nemat-Nasser, S. and Hori, M. (2013) Micromechanics: Overall Properties of Heterogeneous Materials, Volume 37. Elsevier.

[22] Mura, T. (1982) General Theory of Eigenstrains. In: Mura, T., Ed., *Micromechanics of Defects in Solids*, Springer, 1-62. https://doi.org/10.1007/978-94-011-9306-1_1

[23] Milton, G. and Sawicki, A. (2003) Theory of Composites. Cambridge Monographs on Applied and Computational Mathematics. *Applied Mechanics Reviews*, **56**, B27-B28. https://doi.org/10.1115/1.1553445

[24] Caré, S. and Hervé, E. (2004) Application of a N-Phase Model to the Diffusion Coef-

ficient of Chloride in Mortar. *Transport in Porous Media*, **56**, 119-135. https://doi.org/10.1023/b:tipm.0000021730.34756.40

[25] Herve, E. (2002) Thermal and Thermoelastic Behaviour of Multiply Coated Inclusion-Reinforced Composites. *International Journal of Solids and Structures*, **39**, 1041-1058. https://doi.org/10.1016/s0020-7683(01)00257-8

[26] Weng, G.J. (1990) The Theoretical Connection between Mori-Tanaka's Theory and the Hashin-Shtrikman-Walpole Bounds. *International Journal of Engineering Science*, **28**, 1111-1120. https://doi.org/10.1016/0020-7225(90)90111-u

[27] Guan, Z.Z., Zhang, H.C., Gao, Y., Song, P.F., Li, Y., Wu, L.P., *et al.* (2023) Experimental-Computational Investigation of the Elastic Modulus of Mortar under Sulfate Attack. *Materials*, **16**, Article 6167. https://doi.org/10.3390/ma16186167

[28] Asadi, I., Ji, G. and Baghban, M.H. (2023) Evaluating the Effective Thermal Conductivity of Cement Mortar through X-Ray Scanning. *Case Studies in Thermal Engineering*, **41**, Article ID: 102686. https://doi.org/10.1016/j.csite.2022.102686

[29] Baghbani, A., Abuel-Naga, H. and Shirkavand, D. (2023) Accurately Predicting Quartz Sand Thermal Conductivity Using Machine Learning and Grey-Box AI Models. *Geotechnics*, **3**, 638-660. https://doi.org/10.3390/geotechnics3030035

[30] Mondal, P., Shah, S.P. and Marks, L.D. (2009) Nanomechanical Properties of Interfacial Transition Zone in Concrete. In: Bittnar, Z., Bartos, P.J.M., Němeček, J., Šmilauer, V. and Zeman, J., Eds., *Nanotechnology in Construction* 3, Springer, 315-320. https://doi.org/10.1007/978-3-642-00980-8_42

[31] Nguyen, V.T., Lee, S.Y., Yoon, S. and Kim, D.J. (2024) A Comprehensive Study on Predicting the Elastic Modulus and Poisson Ratio of Hardened Cement Pastes via Micro-Scale Cement Hydration Simulations. *Case Studies in Construction Materials*, **20**, e03285. https://doi.org/10.1016/j.cscm.2024.e03285

[32] Ghabezloo, S. (2010) Association of Macroscopic Laboratory Testing and Micromechanics Modelling for the Evaluation of the Poroelastic Parameters of a Hardened Cement Paste. *Cement and Concrete Research*, **40**, 1197-1210. https://doi.org/10.1016/j.cemconres.2010.03.016

[33] Bentz, D.P. (2007) Transient Plane Source Measurements of the Thermal Properties of Hydrating Cement Pastes. *Materials and Structures*, **40**, 1073-1080. https://doi.org/10.1617/s11527-006-9206-9

[34] Hochstein, D.P. and Meyer, C. (2016) Measurement and Prediction of Thermal Conductivity of Cement Paste. *ACI Materials Journal*, **113**, 317-322.

[35] Zhang, H., Xu, Y., Gan, Y., Schlangen, E. and Šavija, B. (2020) Experimentally Validated Meso-Scale Fracture Modelling of Mortar Using Output from Micromechanical Models. *Cement and Concrete Composites*, **110**, Article ID: 103567. https://doi.org/10.1016/j.cemconcomp.2020.103567

[36] Gao, Y.Y., Hu, C.L., Zhang, Y.M., Li, Z.J. and Pan, J.L. (2018) Characterisation of the Interfacial Transition Zone in Mortars by Nanoindentation and Scanning Electron Microscope. *Magazine of Concrete Research*, **70**, 965-972. https://doi.org/10.1680/jmacr.17.00161

[37] Garboczi, E.J. and Bentz, D.P. (1997) Analytical Formulas for Interfacial Transition Zone Properties. *Advanced Cement Based Materials*, **6**, 99-108. https://doi.org/10.1016/s1065-7355(97)90016-x

[38] Nadeau, J.C. (2002) Water-Cement Ratio Gradients in Mortars and Corresponding Effective Elastic Properties. *Cement and Concrete Research*, **32**, 481-490. https://doi.org/10.1016/s0008-8846(01)00710-4

[39] Barthélémy, J.-F. (2024) Echoes: Extended Calculator of HOmogEnization Schemes.

[40] Benveniste, Y., Dvorak, G.J. and Chen, T. (1991) On Diagonal and Elastic Symmetry of the Approximate Effective Stiffness Tensor of Heterogeneous Media. *Journal of the Mechanics and Physics of Solids*, **39**, 927-946. https://doi.org/10.1016/0022-5096(91)90012-d

Appendix A. Eshelby Tensor of a Spheroidal Inclusion and Orientation Averaging

A.1. Components of the Eshelby Tensor

Let the spheroid have semi-axes $a_1 = a_2 = a$ and $a_3 = c$, with aspect ratio $\omega = c/a$ as defined in Equation (75), the axis $\boldsymbol{e}_3$ being the axis of revolution. The matrix is isotropic with Poisson's ratio ν_0. Introducing the geometrical function

$$g(\omega) = \begin{cases} \dfrac{\omega}{\left(1-\omega^2\right)^{3/2}}\left[\arccos\omega - \omega\sqrt{1-\omega^2}\right], & \omega < 1 \quad (\text{oblate}), \\ \dfrac{\omega}{\left(\omega^2-1\right)^{3/2}}\left[\omega\sqrt{\omega^2-1} - \operatorname{arcosh}\omega\right], & \omega > 1 \quad (\text{prolate}), \end{cases} \tag{80}$$

with $g \to 2/3$ as $\omega \to 1$, the non-zero components of the Eshelby tensor read [22]

$$S_{1111} = S_{2222} = \frac{3}{8(1-\nu_0)}\frac{\omega^2}{\omega^2-1} + \frac{1}{4(1-\nu_0)}\left[1-2\nu_0 - \frac{9}{4\left(\omega^2-1\right)}\right]g, \tag{81}$$

$$S_{3333} = \frac{1}{2(1-\nu_0)}\left\{1-2\nu_0 + \frac{3\omega^2-1}{\omega^2-1} - \left[1-2\nu_0 + \frac{3\omega^2}{\omega^2-1}\right]g\right\}, \tag{82}$$

$$S_{1122} = S_{2211} = \frac{1}{4(1-\nu_0)}\left\{\frac{\omega^2}{2\left(\omega^2-1\right)} - \left[1-2\nu_0 + \frac{3}{4\left(\omega^2-1\right)}\right]g\right\}, \tag{83}$$

$$S_{1133} = S_{2233} = \frac{1}{2(1-\nu_0)}\left\{-\frac{\omega^2}{\omega^2-1} + \frac{1}{2}\left[\frac{3\omega^2}{\omega^2-1} - (1-2\nu_0)\right]g\right\}, \tag{84}$$

$$S_{3311} = S_{3322} = \frac{1}{2(1-\nu_0)}\left\{-(1-2\nu_0) - \frac{\omega^2+1}{\omega^2-1} + \frac{1}{2}\left[2(1-2\nu_0) + \frac{3\left(\omega^2+1\right)}{\omega^2-1}\right]g\right\}, \tag{85}$$

$$S_{1212} = \frac{1}{4(1-\nu_0)}\left\{\frac{\omega^2}{2\left(\omega^2-1\right)} + \left[1-2\nu_0 - \frac{3}{4\left(\omega^2-1\right)}\right]g\right\}, \tag{86}$$

$$S_{1313} = S_{2323} = \frac{1}{4(1-\nu_0)}\left\{1-2\nu_0 - \frac{\omega^2+1}{\omega^2-1} - \frac{1}{2}\left[1-2\nu_0 - \frac{3\left(\omega^2+1\right)}{\omega^2-1}\right]g\right\}. \tag{87}$$

The remaining components follow from the minor symmetries $S_{ijkl} = S_{jikl} = S_{ijlk}$; note that $S_{ijkl} \neq S_{klij}$ in general, so the Eshelby tensor of a non-spherical inclusion does not possess the major symmetry.

For $\omega \to 1$, expressions (81)-(87) degenerate into the isotropic sphere result of Equation (6),

$$S_{1111} = \frac{7-5\nu_0}{15(1-\nu_0)}, \quad S_{1122} = \frac{5\nu_0-1}{15(1-\nu_0)}, \quad S_{1212} = \frac{4-5\nu_0}{15(1-\nu_0)}, \tag{88}$$

while $\omega \to \infty$ recovers the cylindrical fibre solution and $\omega \to 0$ the penny-

shaped crack solution.

Numerical note. Equations (81)-(87) are indeterminate at $\omega = 1$ and ill-conditioned in its vicinity, since $g - 2/3$ and $\omega^2 - 1$ both vanish. In the implementation used here, Equation (6) is substituted whenever $|\omega - 1| < 10^{-3}$, and the continuity of the computed curves across this switch has been verified.

A.2. Localization Tensor and Orientation Averaging

In the local frame of the inclusion, the Hill tensor and the dilute strain localization tensor are given by Equations (10) and (12),

$$\mathbb{P}(\omega) = \mathbb{S}(\omega) : \mathbb{C}_0^{-1}, \quad \mathbb{A}^{\text{dil}}(\omega) = \left[\mathbb{I} + \mathbb{P}(\omega) : (\mathbb{C}_i - \mathbb{C}_0)\right]^{-1}. \tag{89}$$

For a uniform (isotropic) orientation distribution, the orientation average of any fourth-order tensor $\mathbb{T}$ possessing the minor symmetries is itself isotropic and is fully determined by two invariants:

$$\langle \mathbb{T} \rangle = \alpha\, \mathbb{J} + \beta\, \mathbb{K}, \quad \alpha = \frac{1}{3} T_{iijj}, \quad \beta = \frac{1}{10}\left(T_{ijij} + T_{ijji} - \frac{2}{3} T_{iijj} \right). \tag{90}$$

Applying (90) to $\mathbb{A}^{\text{dil}}$ yields the two scalars a_i^J and a_i^K of inclusion family i. Because the phases are individually isotropic, the tensor $\mathbb{C}_i - \mathbb{C}_0$ is invariant under rotation, and the Mori-Tanaka estimate (19) reduces, for randomly oriented spheroids, to the two decoupled scalar relations

$$k_{\text{eff}} = k_0 + \frac{\sum_i f_i (k_i - k_0) a_i^J}{f_0 + \sum_j f_j a_j^J}, \quad \mu_{\text{eff}} = \mu_0 + \frac{\sum_i f_i (\mu_i - \mu_0) a_i^K}{f_0 + \sum_j f_j a_j^K}, \tag{91}$$

from which $\tilde{E}$ follows through Equation (28). Setting $\omega = 1$ makes a_i^J and a_i^K equal to the scalar factors implicit in Equations (25)-(26), so that (91) contains the spherical case as a particular instance.

The second-order counterpart used for conduction is obtained in the same way: the orientation average of the diagonal localization tensor of Equation (77) is simply $\langle A^{\text{dil}} \rangle = \frac{1}{3} A_{ii}^{\text{dil}}$, the depolarization factors N_i of Equation (76) playing, for the scalar transport problem, the role held by $\mathbb{S}$ in elasticity. This formal correspondence—a single scalar N_i against a fourth-order tensor with two independent invariants a^J and a^K—is the geometrical expression of the one-channel versus two-channel argument developed in Section 6.

Appendix B. Coefficients of the Deviatoric Problem

B.1. Definition of the Minors $Z_{\alpha\beta}$

Continuity of u_r, u_θ, σ_{rr} and $\sigma_{r\theta}$ at each interface gives the transfer relation (41), and the accumulated transfer matrix through the two layers is $\boldsymbol{S}^{(2)} = \boldsymbol{T}^{(2)} \boldsymbol{T}^{(1)}$ as in Equation (42). The quantities entering Equations (45)-(47) are the second-order minors of this accumulated matrix,

$$Z_{\alpha\beta} = S_{\alpha 1}^{(2)} S_{\beta 2}^{(2)} - S_{\beta 1}^{(2)} S_{\alpha 2}^{(2)}, \quad \alpha, \beta \in \{1, 2, 3, 4\}, \tag{92}$$

so that Z_{12} and Z_{22} are built from the first two columns of $\boldsymbol{S}^{(2)}$ only. Definition (92) is what makes Equations (45)-(47) computable; it is the general n-layer form [16] and applies unchanged to the two-layer case treated here.

B.2. Equivalent Explicit Form for the Two-Layer Inclusion

For the particular case of a single coating, the minors (92) can be eliminated analytically and the equation for μ_{eff} admits the explicit form derived by Christensen and Lo [12]. It is reproduced here as an independent check on the implementation of Equations (43)-(47). Note that this form is established in the convention $Ax^2+2Bx+C=0$, whereas Equation (43) uses $Ax^2+Bx+C=0$; the coefficient B therefore differs by a factor of two between the two sets, and the two must not be mixed.

Writing the core as phase 1 (μ_1, ν_1) and the ITZ shell as phase 2 (μ_2, ν_2), and introducing $m=\mu_1/\mu_2$ and $c=\left(R_1/R_2\right)^3=f_1$, the effective shear modulus is the root of

$$A\left(\frac{\mu_{\text{eff}}}{\mu_2}\right)^2+2B\left(\frac{\mu_{\text{eff}}}{\mu_2}\right)+C=0,\quad \frac{\mu_{\text{eff}}}{\mu_2}=\frac{-B+\sqrt{B^2-AC}}{A}, \tag{93}$$

with

$$\begin{aligned}A=&\,8(m-1)(4-5\nu_2)\eta_1c^{10/3}-2\left[63(m-1)\eta_2+2\eta_1\eta_3\right]c^{7/3}\\&+252(m-1)\eta_2c^{5/3}-50(m-1)\left(7-12\nu_2+8\nu_2^2\right)\eta_2c+4(7-10\nu_2)\eta_2\eta_3,\end{aligned} \tag{94}$$

$$\begin{aligned}B=&-4(m-1)(1-5\nu_2)\eta_1c^{10/3}+4\left[63(m-1)\eta_2+2\eta_1\eta_3\right]c^{7/3}\\&-504(m-1)\eta_2c^{5/3}+150(m-1)(3-\nu_2)\nu_2\eta_2c+3(15\nu_2-7)\eta_2\eta_3,\end{aligned} \tag{95}$$

$$\begin{aligned}C=&\,4(m-1)(5\nu_2-7)\eta_1c^{10/3}-2\left[63(m-1)\eta_2+2\eta_1\eta_3\right]c^{7/3}\\&+252(m-1)\eta_2c^{5/3}+25(m-1)\left(\nu_2^2-7\right)\eta_2c-(7+5\nu_2)\eta_2\eta_3,\end{aligned} \tag{96}$$

where

$$\begin{aligned}\eta_1&=(m-1)(49-50\nu_1\nu_2)+35m(\nu_1-2\nu_2)+35(2\nu_1-\nu_2),\\\eta_2&=5\nu_1(m-1)+7(m+4),\\\eta_3&=m(8-10\nu_2)+(7-5\nu_2).\end{aligned} \tag{97}$$

Two consistency checks are performed in the implementation: $c\to 0$ returns $\mu_{\text{eff}}=\mu_2$ (inclusion entirely made of ITZ material) and $c\to 1$ returns $\mu_{\text{eff}}=\mu_1$ (vanishing ITZ), in agreement with the corresponding limits of the bulk modulus in Equation (38) and of the conductivity in Equation (66).